Atmos. Chem. Phys., 6, 1435–1453, 2006
www.atmos-chem-phys.net/6/1435/2006/


Atmospheric Chemistry and Physics

# Concentrations of OH and $HO_2$ radicals during NAMBLEX: measurements and steady state analysis

**S. C. Smith[1], J. D. Lee[2], W. J. Bloss[1], G. P. Johnson[1], T. Ingham[1], and D. E. Heard[1]**

[1]School of Chemistry, University of Leeds, Leeds, LS2 9JT, UK
[2]Department of Chemistry, University of York, Heslington, York, YO10 5DD, UK

Received: 19 September 2005 – Published in Atmos. Chem. Phys. Discuss.: 28 November 2005
Revised: 8 February 2006 – Accepted: 8 February 2006 – Published: 4 May 2006

**Abstract.** OH and $HO_2$ concentrations were measured simultaneously at the Mace Head Atmospheric Research Station in the summer of 2002 during the NAMBLEX (North Atlantic Marine Boundary Layer EXperiment) field campaign. OH was measured by laser-induced fluorescence employing the FAGE (Fluorescence Assay by Gas Expansion) technique, with a mean daytime detection limit of $2.7\times10^5$ molecule $cm^{-3}$ (5 min acquisition period; signal-to-noise ratio = 1). $HO_2$ was detected as OH following its chemical conversion through addition of NO, with a mean detection limit of $4.4\times10^6$ molecule $cm^{-3}$. The diurnal variation of OH was measured on 24 days, and that of $HO_2$ on 17 days. The local solar noon OH concentrations ranged between (3–8)$\times10^6$ molecule $cm^{-3}$, with a 24 h mean concentration of $9.1\times10^5$ molecule $cm^{-3}$. The local solar noon $HO_2$ concentrations were (0.9–2.1)$\times10^8$ molecule $cm^{-3}$ (3.5–8.2 pptv), with a 24 h mean concentration of $4.2\times10^7$ molecule $cm^{-3}$ (1.6 pptv). $HO_2$ radicals in the range (2–3)$\times10^7$ molecule $cm^{-3}$ were observed at night. During NAMBLEX, a comprehensive suite of supporting measurements enabled a detailed study of the behaviour of $HO_x$ radicals under primarily clean marine conditions. Steady state expressions are used to calculate OH and $HO_2$ concentrations and to evaluate the effect of different free-radical sources and sinks. The diurnally averaged calculated to measured OH ratio was 1.04±0.36, but the ratio displays a distinct diurnal variation, being less than 1 during the early morning and late afternoon/evening, and greater than 1 in the middle of the day. For $HO_2$ there was an overprediction, with the agreement between calculated and measured concentrations improved by including reaction with measured IO and BrO radicals and uptake to aerosols. Increasing the concentration of IO radicals included in the calculations to above that measured by a DOAS instrument with an absorption path located mainly over the ocean, reflecting the domination of the inter-tidal region as an iodine source at Mace Head, led to further improvement. The results are compared with previous measurements at Mace Head, and elsewhere in the remote marine boundary layer.

*Correspondence to:* D. E. Heard
(d.e.heard@leeds.ac.uk)

## 1 Introduction

Hydroxyl radicals (OH) are the principal oxidising species in the troposphere, and dominate the daytime removal of most volatile organic compounds (VOCs) (Levy, 1971; Logan et al., 1981). Reaction with OH thus governs the atmospheric lifetime of many species, and hence their potential to contribute to (for example) climate change and ozone depletion. The OH-initiated oxidation of hydrocarbons and CO in the presence of oxides of nitrogen also leads to the generation of ozone, a constituent of photochemical smog. Improving our understanding of the abundance and distribution of OH is thus a key goal of atmospheric chemistry. As the reactivity of OH is high, its concentration is low (of the order of 0.04–0.2 pptv in the sunlit troposphere) and its chemical lifetime is short (0.1–1 s); OH concentrations are therefore determined by local chemical processes rather than transport. Comparison of in situ measurements of $HO_x$ ($OH+HO_2$) with calculations and box model simulations constrained by observations of longer-lived species such as $NO_x$ ($NO+NO_2$), ozone and VOCs can thus be used to test our understanding of these processes, and to validate the chemical mechanisms included in tropospheric models. This paper describes observations and steady-state analyses of marine boundary layer OH and $HO_2$ concentrations measured at Mace Head, Ireland.

In the summer of 2002 the Universities of Leeds, York, East Anglia, Leicester, UMIST (now Manchester), Birmingham, Aberystwyth, Bristol, Cambridge, Edinburgh and the National University of Ireland (NUI) Galway participated in the NAMBLEX (North Atlantic Marine Boundary Layer

Published by Copernicus GmbH on behalf of the European Geosciences Union.

EXperiment) campaign, located at the Mace Head Atmospheric Research Station, near Carna, County Galway on the west coast of Ireland (53°23′ N, 9°54′ W). The Mace Head site has a clean air sector extending from 180 to 300° encompassing the prevailing westerly winds, and the site experiences a range of clean and semi-polluted air masses arriving mainly from the Atlantic but also from the Arctic, Europe and the United Kingdom (Cape et al., 2000; Simmonds et al., 1996). Further details of the NAMBLEX campaign and the Mace Head site can be found in the NAMBLEX overview paper in this issue (Heard et al., 2005).

Mace Head has been the location for several previous field campaigns at which OH and $HO_2$ have been measured (Creasey et al., 1997, 2002; Berresheim et al., 2002) and compared with simulations using constrained numerical box models. In particular, the NAMBLEX project followed on from the EASE96 (East Atlantic Summer Experiment) and EASE97 (Spring) campaigns during which the University of Leeds FAGE (Fluorescence Assay by Gas Expansion) instrument was also deployed for the measurement of OH and $HO_2$. During EASE96 and 97, OH and $HO_2$ were observed with midday concentrations of $(2.0–6.0)\times10^6$ and $(0.5–3.5)\times10^8$ molecule $cm^{-3}$, respectively (Creasey et al., 2002). The OH concentrations correlated well with the OH production rate from ozone photolysis during periods when clean air, originating in the arctic (low $NO_x$), arrived at Mace Head. Carslaw et al. (2002) used a constrained photochemical box model based upon the Master Chemical Mechanism (MCM http://mcm.leeds.ac.uk/MCM) (Carslaw et al., 1999a; Jenkin et al., 1997) to simulate OH and $HO_2$ during EASE97. It was found, on average, that the model substantially overpredicted OH and $HO_2$ by factors of 2.4 and 3.6, respectively, for data obtained between 11:00 and 15:00 GMT. OH was also measured at Mace Head by Chemical Ionisation Mass Spectrometry (CIMS) during the PARFORCE experiment in 1999 (Berresheim et al., 2002). A mean daily maximum OH of $(2.6\pm0.5)\times10^6$ molecule $cm^{-3}$ was observed, but calculations using a simple box model overestimated OH concentrations by an average factor of 8.2.

$HO_x$ measurements at other remote marine boundary layer locations have tended to indicate typical maximum levels of OH of up to $(3.0–6.0)\times10^6$ molecule $cm^{-3}$, and $HO_2$ of up to $(1.0–2.5)\times10^8$ molecule $cm^{-3}$ (ca. 4–10 pptv). Agreement between observed OH and calculations using constrained box-models has been reasonably good with model/measurement ratios of 1.15 (Cape Grim, Tasmania – SOAPEX-2 – Sommariva et al., 2004), 1.17 (South Atlantic – ALBATROSS – Brauers et al., 2001) and 0.80 (Christmas Island, Pacific Ocean – PEM Tropics A – Chen et al., 2001). In contrast, for $HO_2$, models have tended to overestimate the measurements, with reported model/measurement ratios of 1.4 (SOAPEX-2 – Sommariva et al., 2004), 0.8 and 2 (Okinawa and Oki Islands, respectively – ORION-99 – Kanaya et al., 2001a) and 1.7 (Rishiri Island – Kanaya et al., 2002). Given the importance of quantitative prediction of tropospheric $HO_x$ for determination of the atmospheric oxidative capacity, improvements are required in our understanding of the chemistry occurring in (nominally) clean environments such as the remote marine boundary layer.

From the perspective of $HO_x$ chemistry, the NAMBLEX campaign featured several improvements to the data coverage compared with previous studies at Mace Head and elsewhere in the marine boundary layer, notably measurement of a more comprehensive suite of OH sinks, including previously unmeasured oxygenated VOCs (*o*-VOCs) (Lewis et al., 2005), the $HO_2$ co-reactants IO and BrO (Saiz-Lopez et al., 2004a, b, 2005, 2006), and detailed aerosol chemical composition and size distribution measurements (Coe et al., 2005). The OH and $HO_2$ measurements were performed simultaneously rather than sequentially, permitting a more accurate constraint of the flux between the $HO_x$ species. In contrast with the EASE96 and EASE97 campaigns, the measurements of radical species ($NO_3$, $OH/HO_2$, $RO_2$) were co-located at the shoreline site, together with the aerosol, VOC, $O_3$ and meteorological measurements. Previously the instruments had been separated by up to 200 m, leading to concerns that instruments may have sampled different air masses following the formation of an internal boundary layer as the oceanic air encounters the shoreline (Carslaw et al., 2002).

This paper describes the NAMBLEX $HO_x$ measurements and analyses of the OH and $HO_2$ concentrations using the steady-state approximation. Comparisons of the measurements with the predictions of a constrained box model are described in a separate paper (Sommariva et al., 2005). The paper is structured as follows: The basic $HO_x$ photochemical relationships are given in Sect. 2, followed by a description of the experimental technique, including the calibration, precision and accuracy of the FAGE system, in Sect. 3. The OH and $HO_2$ dataset is described in Sect. 4. In Sect. 5, the relationship between OH and the rate of ozone photolysis ($j-(O^1D)$) is considered (Sect. 5.1), followed by an examination of the ability of steady state expressions of increasing complexity to simulate the measured OH (Sect. 5.2) and $HO_2$ (Sect. 5.3) concentrations. Finally, in Sect. 6, the results from NAMBLEX are discussed and placed in the context of related analyses undertaken for similar environments.

## 2 Tropospheric $HO_x$ photochemistry

The major OH production pathway in the troposphere is photolysis of ozone at wavelength of light $\leq$340 nm, followed by reaction of the resulting electronically excited $O^1D$ atoms with water vapour, in competition with their collisional quenching. This primary production rate for OH, P(OH), is given by:

$$P(OH)=2f[O_3]j-(O^1D) \quad (1)$$

where $j-(O^1D)$ is the rate of $O_3$ photolysis by sunlight to generate $O^1D$ and $f$ is the fraction of $O^1D$ that reacts with

water vapour to produce OH, rather than undergoing collisional quenching with $N_2$, $O_2$ or $H_2O$ to form $O^3P$:

$$f = \frac{k_{O^1D+H_2O}[H_2O]}{k_{O^1D+H_2O}[H_2O] + k_{O^1D+N_2}[N_2] + k_{O^1D+O_2}[O_2]} \quad (2)$$

Under normal mid-latitude marine boundary layer conditions $f$ takes values of around 0.1–0.2 (minor quenching species, such as $CO_2$, are neglected).

The major sinks for OH under clean conditions are CO, $CH_4$ and VOCs, resulting in production of $HO_2$ and other peroxy radicals ($RO_2$). $HO_2$ is also produced through reaction of OH with $O_3$ and photolysis of HCHO, and is recycled to OH through reaction with $O_3$ and NO. $HO_x$ chain termination occurs via radical recombination reactions ($HO_2$+$HO_2$, $HO_2$+$RO_2$ and OH+$HO_2$) and by the reaction of OH with $NO_2$, the former dominating in clean air, the latter in polluted air. The lifetime of OH is typically less than 1 s and consequently OH rapidly reaches photochemical steady state, given by:

$$[OH]_{ss} = \frac{\text{rate of production}}{\sum_i k_{OH+i}[i]} \quad (3)$$

where each $i$ represents an OH co-reactant. If $O_3$ photolysis is the only OH production mechanism, and reaction with CO and $CH_4$ are the only sinks, $[OH]_{ss}$ is given by:

$$[OH]_{ss} = \frac{P(OH)}{k_{OH+CO}[CO] + k_{OH+CH_4}[CH_4]} \quad (4)$$

Equation (4) can be extended to incorporate additional OH sources (e.g., $HO_2$+NO) and sinks (e.g., reaction of OH with $H_2$, $NO_2$ and dimethylsulphide, DMS). Section 5 of this paper assesses how comprehensive a selection of OH precursors and co-reactants is required to satisfactorily simulate measured OH concentrations at Mace Head.

Steady-state calculations of $HO_2$ are more complicated than those of OH, as they must take into account both the fast interconversion with OH, and the second order $HO_2$ removal processes, $HO_2$+$HO_2$ and $HO_2$+$RO_2$. Expressions deriving a relationship between $HO_2$ and the square root of $j-(O^1D)$ have been used previously (e.g., Penkett et al., 1997), but require assumptions regarding the $HO_2$:$RO_2$ ratio and neglect certain $HO_2$ removal terms. In this work, we have adopted the cubic equation for $HO_2$ developed by Carslaw et al. (1999b, 2002):

$$\beta[HO_2]^3 + \gamma[HO_2]^2 + \delta[HO_2] + \varepsilon = 0 \quad (5)$$

where $\beta$, $\gamma$, $\delta$, and $\varepsilon$ are derived from a reduced "mini" mechanism of the MCM (25 reactions and 17 species), and contain measured concentrations of long-lived species, together with radiative and kinetic parameters (see Appendix A). The "mini" mechanism was shown to be valid under clean conditions at Mace Head, with $HO_2$ concentrations calculated from the solution of expression (5) being within 20% of calculations carried out using the full, near-explicit MCM, containing ca. 1500 reactions (Carslaw et al., 1999b, 2002).

## 3 Experimental

OH and $HO_2$ radicals were measured using laser-induced fluorescence (LIF), via the FAGE (Fluorescence Assay by Gas Expansion) technique (Hard et al., 1984; Heard and Pilling, 2003). The instrument used was an improvement of that deployed in previous campaigns (e.g., Creasey et al., 2003), with several significant modifications (described below), notably the use of two detection channels enabling simultaneous (rather than sequential) measurement of OH and $HO_2$, implementation of an all solid state laser system, and use of a fibre-optic system for delivery of the UV radiation to the fluorescence cells. The instrument was housed in an air-conditioned 20 foot shipping container, fitted out as a mobile laboratory. The laser system, fibre launch optics, photon counting electronics, computer and pumping system were located inside the container whereas the fluorescence cells, detectors and gating electronics were housed in a weatherproof box on the container roof.

The FAGE system was located at the "shoreline" measurement site at Mace Head, approximately 50 m horizontally and 10 m vertically (inlet height) from the high-water mark. A plan of the Mace Head site is shown in the NAMBLEX overview paper in this issue (Heard et al., 2005), indicating the relative positions of the various instruments. The fetch from the shoreline was unobstructed by buildings or other instruments. The container was mounted on a flatbed trailer, giving a sampling height ca. 5 m above ground level. A schematic diagram of the overall layout of the instrument is shown in Fig. 1.

### 3.1 Instrumental details

The FAGE technique uses 308 nm on-resonance laser-induced fluorescence to detect OH radicals, employing a low-pressure gas expansion to extend the fluorescence lifetime and permit temporal discrimination between scattered laser light and OH fluorescence. The gas expansion also ensures rapid refreshing of the gas in the fluorescence region, enabling use of a high pulse repetition frequency, low pulse energy excitation laser which minimises any photolytically induced interferences while giving the sensitivity necessary to detect OH at ambient levels. In the Leeds system, ambient air is expanded into two low-pressure fluorescence cells, one of which is used for OH detection, and the other (through addition of NO, and hence conversion of ambient $HO_2$ to OH) for the detection of $HO_2$.

During NAMBLEX, a novel all solid-state, Nd:YAG pumped Ti:Sapphire laser was used to generate 308 nm radiation used for OH excitation, in place of the copper vapour pumped dye laser used previously. A full description of the laser system is given in Bloss et al. (2003); illustrative details will be given here. The pump laser is a diode-pumped, intra cavity doubled, Q-switched, Nd:YAG laser (Photonics Industries DS 20-532), which produces ~10 W

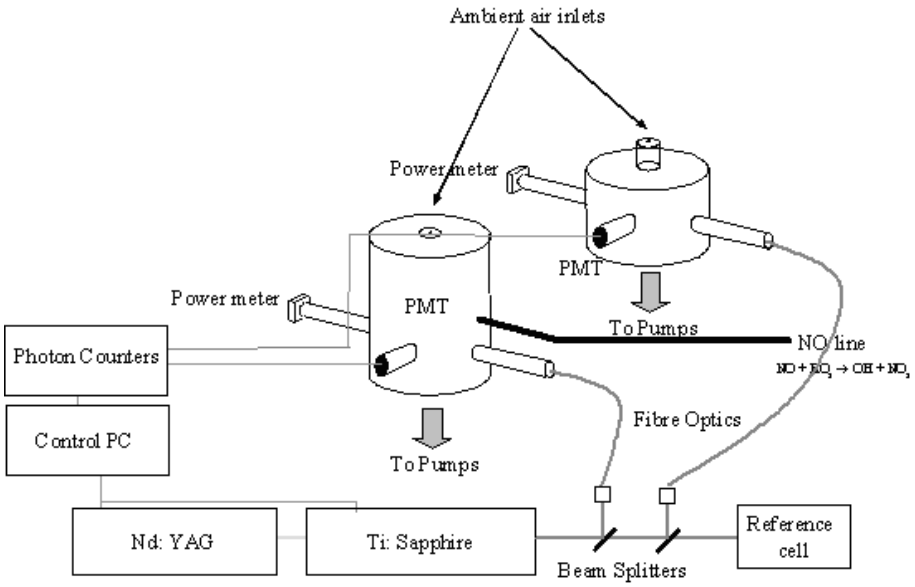


**Fig. 1.** A schematic of the FAGE instrument as deployed during the NAMBLEX campaign.

of 532 nm radiation at a repetition frequency of 5 kHz. The 532 nm radiation is used to pump a water cooled Ti:Sapphire crystal, producing broadband near IR radiation in the range 690–1000 nm. The Ti:Sapphire oscillator wavelength of approximately 924 nm is selected using a diffraction grating, with computer control of the grating angle. The fundamental wavelength from the Ti:Sapphire is then passed through two non-linear harmonic generation stages consisting of two cerium lithium borate crystals, producing 462 nm and 308 nm radiation by second and third harmonic generation, respectively. The beam profile produced by the laser cavity design contains a number of longitudinal modes such that following harmonic generation, a spectral linewidth of $\sim$0.065 $cm^{-1}$ is produced, thus providing efficient overlap with the Doppler broadened OH spectral profile at 308 nm under the low pressure conditions of the FAGE instrument (approximately 0.08 $cm^{-1}$). The $Q_1(2)$ branch of the OH $A^2\Sigma^+$ ($v'$=0) – $X^2\Pi_i$ ($v''$=0) transition was excited at 307.999 nm. Approximate ($\pm$0.002 nm) wavelength tuning is provided by splitting a small fraction of the second harmonic radiation into a wavemeter. Precise tuning to the peak of the spectral line of OH is then achieved by use of a reference fluorescence cell containing a high [OH] (produced by a microwave discharge of water vapour in ambient air at 5 Torr). Upon exiting the laser, the UV radiation is passed through a series of dielectric beamsplitters and split into three fractions of 5%, 25% and 70% power. The 5% fraction of the radiation is directed into the reference cell for wavelength calibration. The 70% and 25% fractions are focussed into fibre optic cables (length=5 m) for transmission of the light into the OH and $HO_2$ measurement cells, respectively, positioned on the roof of the container. Upon exiting the fibres, the light is collimated using a plano-convex lens, and passed through the detection cells via baffled side arms, providing a 10 mm diameter laser beam in the excitation region. The total light transmission through the fibre optic system from the beamsplitter to the centre of the detection cell was $\sim$60%. After traversing each cell, the laser beam exits via a second baffled side-arm and is directed onto a UV sensitive photodiode, enabling the laser power in each cell to be monitored continuously for subsequent normalisation of the OH LIF signal for any fluctuations in laser power. Typically, the laser power entering the OH and $HO_2$ detection chambers was $\sim$20 mW and $\sim$5 mW, respectively.

The detection cells comprised 220 mm internal diameter cylindrical chambers, with internal surfaces sand blasted to minimise reflections. Each cell pressure was monitored by a capacitance manometer, and was independently adjustable through butterfly valves located at the cell exit prior to the roots/rotary pumping system. The nozzle arrangement differed for OH and $HO_2$ to maximise OH sensitivity and $HO_2$ conversion efficiency, respectively. For the OH cell, ambient air was expanded through a 0.8 mm flat nozzle, with a flow rate of ca. 4.8 slm, into the fluorescence chamber held at a pressure of 0.9 Torr. The gas expansion intersected the laser and detection axes approximately 90 mm below the nozzle. The $HO_2$ cell had a reduced nozzle diameter of 0.6 mm (total flow rate into the cell was ca. 3.6 slm), an increased nozzle to laser-axis distance of 400 mm, and featured an NO injection ring positioned concentrically around the gas beam, $\sim$250 mm below the nozzle. The injection of NO well downstream of the initial gas expansion (containing the supersonic region) resulted in better mixing of the NO with the gas stream, compared with injection directly beneath the nozzle.

NO was injected with a flow of 140 sccm into the beam, resulting in conversion of approximately 75% of the ambient $HO_2$ to OH. The OH and $HO_2$ cell inlets were separated horizontally by approximately 70 cm. The LIF signal from the $HO_2$ channel arises from OH converted from ambient $HO_2$ plus ambient OH.

The fluorescence collection axes, perpendicular to the laser beam, comprise collimating lenses, a narrow bandwidth interference filter (transmission >50% at 308 nm, FWHM=8.0 nm) and focussing lenses to direct the 308 nm radiation onto the 8 mm diameter photocathode of a channeltron photomultiplier (CPM). The solid angle of fluorescence collected was approximately doubled using a spherical mirror mounted opposite the collection optics. The CPM was switched off $\sim$2 $\mu$s before the laser pulse using a gating system developed at Leeds (Creasey et al., 1998) to provide a +100 V potential difference on the cathode relative to the channeltron body. The CPM is held in this low gain state until $\sim$100 ns after the peak of the laser pulse. The CPM is then switched back to the high gain state in order to collect the OH fluorescence signal. The CPM signal is amplified and recorded using photon counting techniques, during a 500 ns wide integration window, commencing 100 ns after the peak of the laser pulse. A second integration window, delayed 50 $\mu$s after the laser pulse with a width of 5 $\mu$s, was used to measure the signal from solar scattered light entering the chamber through the nozzle, for subsequent subtraction.

The computer controlled data acquisition sequence in the OH cell is as follows: (1) The centre of the $Q_1(2)$ line is located by scanning the laser wavelength across a 0.005 nm region encompassing the peak of the line whilst recording the reference cell signal, and then adjusting the wavelength to the line peak (such that the reference cell signal reached at least 90% of its maximum). (2) The wavelength is then kept constant for a period of 200 s (consisting of 10 points, where 1 data point is acquired every 20 s), during which the sum of laser scatter and OH fluorescence signal (with the contribution from solar scatter subtracted) is recorded. (3) The wavelength is then stepped down by 0.005 nm, so that the laser is no longer on-resonance with the OH spectral line, allowing the signal solely due to laser scattered light to be collected for subsequent subtraction. This background signal is collected for 100 s (5 points of 20 s averaging). (4) The OH fluorescence signal is then normalised to laser power using the signal from the UV photodiode situated after the exit arm of the cell. For the $HO_2$ cell, the data acquisition sequence is the same as for the OH cell, but NO is added to the chamber. The flow of NO is switched off part way through the background points (laser not on resonance with OH) to check for any increased background due to the presence of NO (which was not observed). A small (<5%) correction was required as the "$HO_2$" cell signal contains a contribution due to ambient OH; this was subtracted using the OH concentration determined in the other cell, adjusted for the relative OH sensitivities between the cells.

### 3.2 Calibration

[OH] sampled at the nozzle is directly related to the observed signal, $S$, by a calibration constant, $C_{OH}$, and the laser power, $P$:

$$S = C_{OH} P [OH] \quad (6)$$

$C_{OH}$ cannot be calculated accurately as it depends on parameters that are hard to measure such as the optical collection and sampling efficiency. $C_{OH}$ was therefore determined empirically using the $H_2O$ photolysis/$O_3$ actinometry method (Schultz et al., 1995). Briefly, synthetic air with a known concentration of $H_2O$ (determined by an infra-red absorption spectrometer with a precision and accuracy of 0.02% v/v, and a response time of 5 s), was flowed at 12 slm through a quartz flow tube (0.6 m long, 22 mm internal diameter) held vertically above the inlet nozzle. The air was exposed to 184.9 nm radiation from a mercury pen-ray lamp with an axial irradiation zone of length 23 mm. The centre of the irradiation zone is 64 mm above the inlet nozzle, with a transit time to the nozzle of ca. 0.1 s. Photolysis of water vapour at 184.9 nm leads to the production of OH radicals and H atoms. $HO_2$ radicals are rapidly formed by the reaction of H atoms with ambient $O_2$. The OH and $HO_2$ production was quantified relative to the concomitant formation of $O_3$ following the photolysis of $O_2$ :

$$H_2O + h\nu \rightarrow OH + H \quad (R1)$$

$$H + O_2 + M \rightarrow HO_2 + M \quad (R2)$$

$$O_2 + h\nu \rightarrow 2O \quad (R3)$$

$$2(O + O_2 + M \rightarrow O_3 + M) \quad (R4)$$

Approximately 4.8 slm of the calibration gas was sampled through the inlet nozzle (3.6 slm in the case of the $HO_2$ cell), with the remaining gas forming an excess flow, in which $O_3$ was measured using a UV photometric detector (precision and accuracy of $\pm$0.6 ppbv and detection limit of 0.4 ppb for 1 min averaging), enabling [OH] and [$HO_2$] to be calculated through knowledge of the relevant quantum yields and cross sections:

$$[OH] = [HO_2] = \frac{[O_3][H_2O]\sigma_{184.9\,nm(H_2O)}\phi_{HO_x}}{[O_2]\sigma_{184.9\,nm(O_2)}\phi_{O_3}} \quad (7)$$

where $\phi_{OH}$=$\phi_{HO_2}$=1 and $\phi_{O_3}$=2 are the quantum yields for production of OH, $HO_2$ and $O_3$, respectively. The ozone concentration used to calculate the OH level at the inlet nozzle, via Eq. (7), was corrected by a profile factor, which accounts for the variation in axial velocity across the laminar flow in the calibration tube, defined as $[O_3]_{excess}/[O_3]_{centre}$, which was determined experimentally to be 1.94$\pm$0.07. Several studies have shown that the effective absorption cross section of $O_2$ at 185 nm depends on the individual photolysis lamp used (and its operating conditions) and the $O_2$ column

through which the radiation propagates (Cantrell et al., 1997; Creasey et al., 2000; Hofzumahaus et al., 1997) and as a result $\sigma_{184.9\,nm(O_2)}$ was measured for the actual lamp and operating conditions used in the field calibrations.

OH and $HO_2$ calibrations were carried out daily during the NAMBLEX campaign. The calibration constants for both the OH and $HO_2$ cells were insensitive to changes in water vapour under the (moist) conditions typically experienced at Mace Head ($H_2O$=0.5–2.2% v/v). As a result, the daily calibrations were carried out using a $H_2O$ mixing ratio of ca. 0.7% and $O_3 \sim 2.5$ ppbv, resulting in [OH] and [$HO_2$] levels of the order of $10^9$ molecule $cm^{-3}$. In separate tests, multipoint calibrations, involving attenuation and measurement of the relative 184.9 nm flux, and carried out at constant [$H_2O$], have demonstrated that the instrument has a linear response to [OH] and [$HO_2$] in the range $10^7$–$10^9$ molecule $cm^{-3}$, and thus the daily calibration was applicable to atmospheric levels of [OH] and [$HO_2$]. During NAMBLEX, the mean OH calibration constant $C_{OH}$ was $(1.76\pm0.38)\times10^{-7}$ cts molecule$^{-1}$ $cm^3$ $s^{-1}$ $mW^{-1}$. The analogous $HO_2$ calibration constant $C_{HO_2}$ was $(3.28\pm1.21)\times10^{-8}$ cts molecule$^{-1}$ $cm^3$ $s^{-1}$ $mW^{-1}$ (where the mean $C_{OH}$ for the $HO_2$ cell was $(4.30\pm0.84)\times10^{-8}$ cts molecule$^{-1}$ $cm^3$ $s^{-1}$ $mW^{-1}$). The difference arises as a consequence of the incomplete conversion of $HO_2$ to OH, and the differences in expansion jet geometry between the cells. $C_{HO_2}$ was determined either by converting the OH in the calibration flow-tube to $HO_2$ via the addition of CO, or by measuring the additional OH LIF signal when NO was added to the $HO_2$ cell, giving very similar results.

Assuming Poisson statistics, the lower detection limit for OH is given by (Stevens et al., 1994; Holland et al., 1995):

$$[\mathrm{OH}]_{\min}=\frac{S/N}{CP}\sqrt{\left(\frac{1}{m}+\frac{1}{n}\right)}\sigma_b \quad (8)$$

$$\sigma_b=\sqrt{\frac{1}{t}\left(S_{lb}+S_{sb}+S_{db}\right)} \quad (9)$$

where $S/N$ is the signal-to-noise ratio, $P$ (mW) is the laser power, $m$ is the number of data points of OH signal, $n$ is the number of background data points, $t$ (s) is the averaging time for each data point, and $S_{lb}$, $S_{sb}$, $S_{db}$ (cts $s^{-1}$) are the background signals due to laser scatter, solar scatter and the PMT dark count, respectively. The detection limit was calculated for each day on which measurements were made using Eqs. (7) and (8) with $S/N$=1, $t$=20 s, $S_{db}$=0, $m$=10, $n$=5, actual $S_{lb}$ and $S_{sb}$ from around solar noon, and $C_{OH}$ from the most recent calibration. These daily detection limits were then averaged to give the mean daytime detection limit for [OH] of $(1.91\pm0.64)\times10^5$ molecule $cm^{-3}$ over a 300 s data collection period. At night, the detection limit improved as $S_{sb}$=0 and so the mean night-time detection limit for [OH] was found to be $(6.09\pm2.75)\times10^4$ molecule $cm^{-3}$. The corresponding mean values for [$HO_2$] were found to be $(2.94\pm1.05)\times10^6$ molecule $cm^{-3}$ (0.11 pptv) during the day and $(1.02\pm0.39)\times10^6$ molecule $cm^{-3}$ (0.04 pptv) at night. The accuracy in the reported measurements is determined by the calibration factors and is 22% and 25%, respectively, ($1\sigma$) for OH and $HO_2$. The precision of the instrument (quoted as a percentage) depends upon the signal magnitude (i.e. upon the concentration measured), and is determined by fluctuations in the background signal (solar and laser-induced). The standard deviation of the background signal was 2.6 counts $s^{-1}$, and hence for [OH]=$3\times10^6$ molecule $cm^{-3}$, the precision is 20%, giving a total uncertainty in quadrature of 30%. For [$HO_2$]=$1\times10^8$ molecule $cm^{-3}$ (4 pptv), the corresponding $1\sigma$ uncertainty is 28%.

## 4 Results

### 4.1 Overview of the $HO_x$ data set

During the NAMBLEX campaign OH measurements were made on 24 days between 25 July and 1 September 2002, whilst due to technical difficulties $HO_2$ was only measured on 17 days, between 31 July and 1 September. Figure 2 shows the time series of OH and $HO_2$ for the entire campaign. Each measurement is an average of 10 adjacent 20 s data points within a 5 min data collection cycle (taking into account the background period of 5 adjacent 20 s data points). The corresponding values of $j-(O^1D)$ averaged over 5 min are also shown. OH has a clearly defined diurnal profile with absolute daytime maxima around local solar noon (12:45 GMT at Mace Head) varying between (3–8)$\times10^6$ molecule $cm^{-3}$. Figure 3a shows the average diurnal profile of OH over the entire measurement period. The 24 h mean OH concentration (derived from hourly means) was found to be $9.1\times10^5$ molecule $cm^{-3}$. A diurnal pattern is again exhibited for $HO_2$, although on some days it is less pronounced (for example, Fig. 2, 21 August). Daytime maxima varied between 0.9–2.1$\times10^8$ molecule $cm^{-3}$ ($\sim$3.5–8.2 pptv). Data taken on the night of 31 August–1 September (Fig. 2) provides significant evidence to support the presence of night-time $HO_2$ radicals, with observed concentrations of (2–3)$\times10^7$ molecule $cm^{-3}$ (0.8–1.2 pptv) (c.f. mean $HO_2$ night-time detection limit of $1.8\times10^6$ molecule $cm^{-3}$ (0.04 pptv)) as observed previously at Mace Head (Creasey et al., 2002; Salisbury et al., 2001). Figure 3b shows the average diurnal profile of $HO_2$. The 24 h mean $HO_2$ concentration was found to be $4.2\times10^7$ molecule $cm^{-3}$ (1.7 pptv). Both the OH and $HO_2$ 24 h mean concentrations include relatively few night-time observations, however their abundance is expected to be dominated by daytime values. Analysis of the dependence of the ratio of [$HO_2$]/[OH] on NO was carried out using three NO bins of 0–10, 10–30 and 30–500 pptv for which the ratio [$HO_2$]/[OH] was found to be 119, 73 and 53, respectively. This behaviour is quantitatively similar

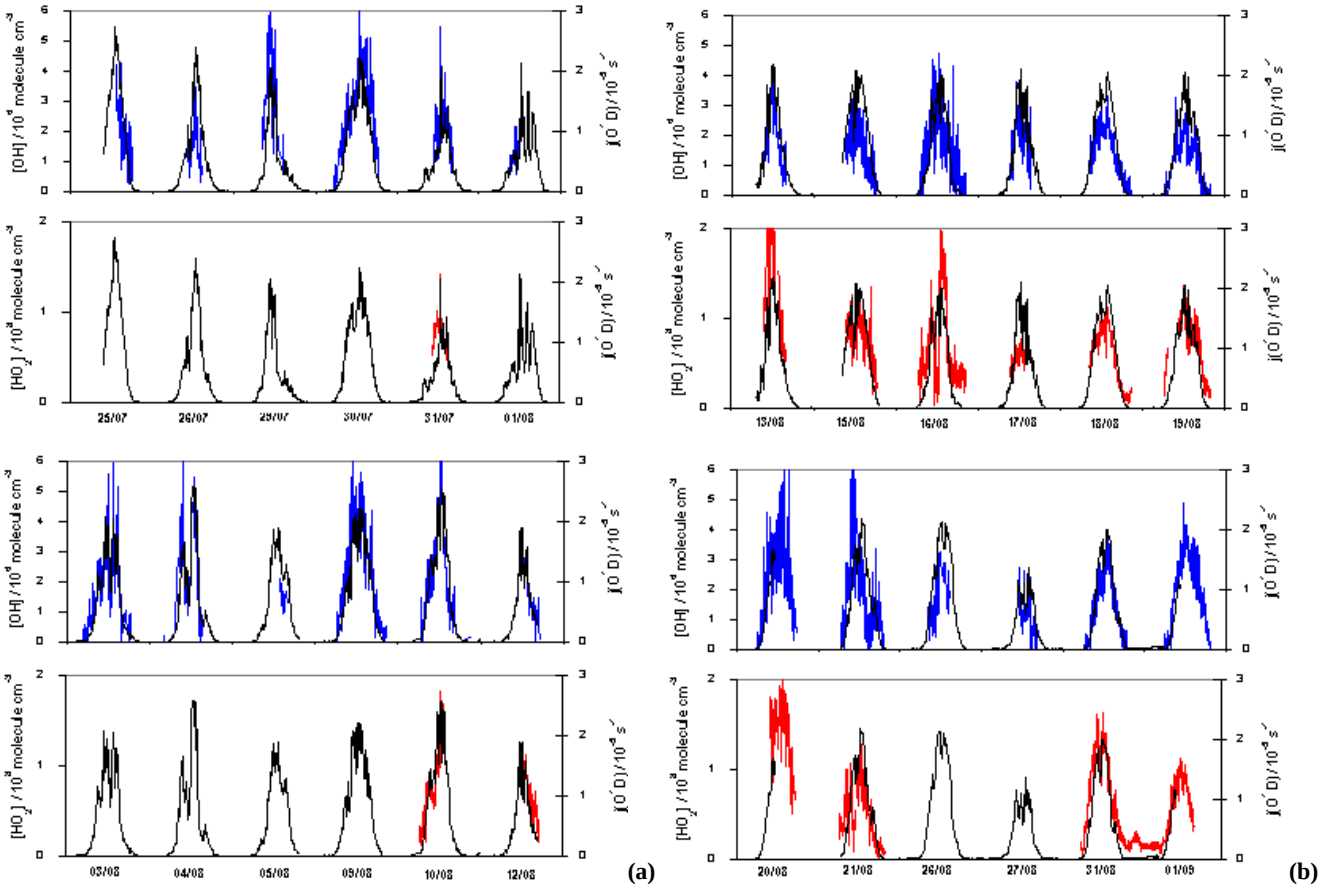


**Fig. 2.** Time-series of OH (blue) and $HO_2$ (red) concentrations during NAMBLEX. Each point represents a 5 min collection period comprising 10 adjacent 20 s online data points with a consecutive background period consisting of 5 adjacent 20 s data points. 5 min averaged $j-(O^1D)$ (black) as measured by a spectral radiometer, are also shown.

to that seen during the EASE97 field campaign which took place at Mace Head when the $[HO_2]/[OH]$ ratio was seen to reduce from 80 to 34 as the average NO level increased from 42 to 279 pptv (Creasey et al., 2002). The data from the campaigns clearly illustrates how the ratio $[HO_2]/[OH]$ falls as NO increases due to the increased rate of recycling of $HO_2$ to OH.

## 5 Data analysis and interpretation

### 5.1 $j-(O^1D)$ dependence of OH

The dependence of OH upon the rate of production of electronically excited oxygen atoms, $j-(O^1D)$, depends upon the chemistry dominating OH production. In the absence of $NO_x$, primary production via $O_3$ photolysis and the subsequent $O^1D+H_2O$ reaction is expected to dominate, and OH should show an approximately linear relationship with $j-(O^1D)$, with some deviation due to $HO_2+O_3$. At higher NO levels, the $HO_2$+NO reaction and HONO photolysis are of increasing importance as sources of OH and the relationship between OH and $j-(O^1D)$ becomes more complex.

In their analysis of OH data acquired at a rural site in Germany, Ehhalt and Rohrer (2000) have shown that for a particular $NO_x$ level the dependence of OH upon $j-(O^1D)$ can be better described by an expression of the form $OH=a\times j-(O^1D)^b$, where the non-unity exponential parameter $b$ incorporates the influences of for example, $j-(NO_2)$ and $j-(HONO)$ upon OH production, via $HO_2$+NO and HONO photolysis, respectively. This analysis was subsequently applied by Berresheim et al. (2003) to OH data acquired during the MINOS campaign on the North Eastern coast of Crete in 2001, where $a$=1.39–2.2 and $b$=0.68, was found to describe their data well.

At Mace Head, radical production from $NO_3$ initiated hydrocarbon oxidation and alkene ozonolysis has been observed previously (Salisbury et al., 2001), consequently we have examined the use of a modification to the expression used by Berresheim et al. (2003) to include an intercept, which can account for non-photolytic OH production:

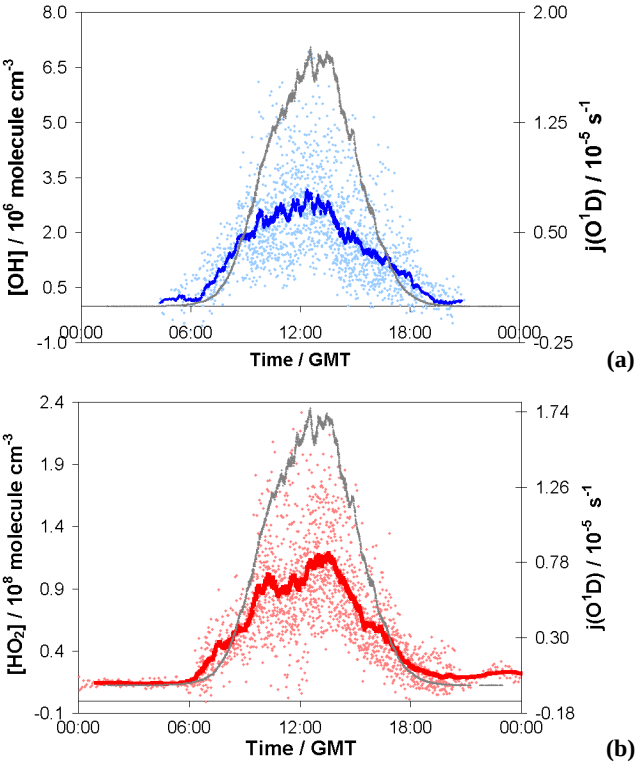


**Fig. 3.** **(a)** Diurnal profile of all OH data (200 s averages) for the campaign (light blue circles), together with a 40 point running mean of the OH data, (dark blue lines) and a campaign averaged $j-(O^1D)$ (grey line). **(b)** Diurnal profile of all $HO_2$ data (200 s averages) for the campaign (pink diamonds), together with a 40 point running mean (red line) and a campaign averaged $j-(O^1D)$ (grey line).

$$[OH]/10^6 \text{ molecule cm}^{-3} = a \times \left(j-(O^1D)/10^{-5}\,\text{s}^{-1}\right)^b + c \quad (10)$$

Inclusion of the intercept should allow a better description of the data during twilight and overnight; also determination of the parameters $a$, $b$ and $c$ from predominantly daytime OH and $j-(O^1D)$ data could constrain the levels of OH anticipated overnight, if the nighttime production mechanisms continue during daylight hours – as expected for alkene ozonolysis but not $NO_3$. The coefficients in Eq. (10) were optimised by least-squares fitting to the observed OH concentrations and $j-(O^1D)$ values, the latter measured by a 2-$\pi$ spectral radiometer (see Heard et al., 2005, this issue, for further details). Fits were performed for a linear form of Eq. (10) ($b$=1, $c$=0) (1), a simple power function ($c$=0) (2), or a power function with an intercept (3), as shown in Table 1. The experimental scatter plot of [OH] versus $j-(O^1D)$ and associated fits with Eq. (10) are shown in Fig. 4. While the improvement in correlation coefficient ($r^2$) between the successive fits is modest (partly reflecting the high scatter of the data when all plotted together), visual inspection of the scatter plot shows that fits (2) and (3) clearly better describe the data than the simple linear fit (1).

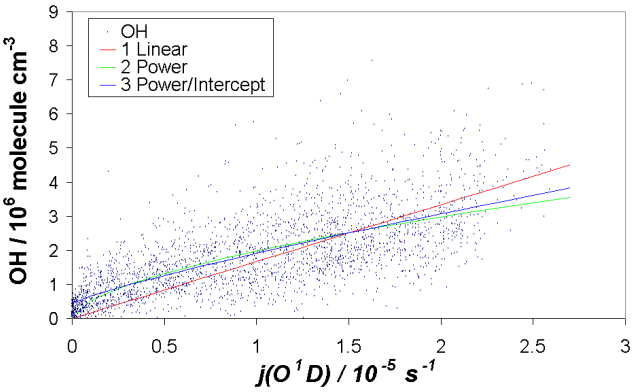


**Fig. 4.** Measured OH data from the NAMBLEX campaign plotted against $j-(O^1D)$ (measured by a spectral radiometer), together with fits to three versions of Eq. (10): (1) Linear (red line), (2) Power (green line) and (3) Power with intercept (blue line). See text for details.

**Table 1.** Fitting Eq. (10) to OH/$j-(O^1D)$ data for the entire campaign, uncertainties are $\pm 1\sigma$.

| Fit | a | b | c | $r^2$ |
|---|---|---|---|---|
| 1 Linear | 1.67±0.02 | 1 (fixed) | 0 (fixed) | 0.404 |
| 2 Power | 1.98±0.02 | 0.59±0.02 | 0 (fixed) | 0.470 |
| 3 Power/Intercept | 1.47±0.08 | 0.84±0.05 | 0.44±0.06 | 0.476 |

The dependence of OH upon $j-(O^1D)$ is itself dependent upon $NO_x$, as noted by Ehhalt and Rohrer (2000). During NAMBLEX, the envelope of $NO_x$ (ca. 5–2000 pptv) encompassed the range from "clean" to "polluted" conditions, such that single values for $a$, $b$ and $c$ are not necessarily applicable to the entire dataset. We have therefore repeated the fitting analysis, with the data in three NO bins, covering 0–10, 10–30 and 30–500 pptv (the latter bin approximately equivalent to the conditions during MINOS). The resulting optimised parameters are given in Table 2.

In all cases addition of the power-dependence upon $j-(O^1D)$ results in a better fit than the simple linear expression, with the improvement most marked in the 30–500 ppt NO bin, which corresponds to "intermediate" $NO_x$ conditions, with recycling of $HO_2$ to OH mediated by the $HO_2$+NO reaction, and deviation from a simple OH/$j-(O^1D)$ correlation is expected. In general the exponent $b$ is less than 1, corresponding to a "concave" fit to the data, and reflecting the fact that OH rises more rapidly than $j-(O^1D)$ (on average) at low $j-(O^1D)$, possibly due to contributions to $HO_x$ from photolysis of reservoir species such as HONO and/or HCHO, which will have relatively higher photolysis rates at high solar zenith angles (SZA) than for ozone.

In comparison with the results of Berresheim et al. (2003) during the MINOS campaign (a marine environment on Crete), we find the value of $b$ to be lower for the 30–500 pptv NO bin which is most comparable to the MINOS conditions (during which $NO_2$ ranged from 60–1040 pptv): NAMBLEX, $b$=0.56±0.03; MINOS, $b$=0.68±0.01, but the value of $a$ to be slightly higher (NAMBLEX, $a$=2.29±0.04; MINOS, $a$=1.39, 1.71 and 2.20 for different time periods). The difference in values of $b$ suggests that non-primary production of OH was more important for Mace Head during NAMBLEX than for Crete during MINOS (also reflected in the much higher scatter apparent in Fig. 4, compared with the equivalent plot for the MINOS dataset). The parameter $a$ relates the steady-state OH level to the solar intensity; during NAMBLEX, typical ozone levels were less than MINOS (approximately 30 vs. 60 ppbv) while the conversion of $O^1D$ to OH was roughly equivalent, thus observation of a comparable value for $a$ may suggest that the OH reactivity (the rate at which it is removed by sinks) was rather higher in the Mediterranean environment of MINOS than in the North Eastern Atlantic environment of NAMBLEX.

Interestingly, addition of the third, intercept parameter $c$ results in little or no improvement to the fits, suggesting that non-photolytic radical production was relatively unimportant over this time period at Mace Head. In the case of the low NO bins, 0–10 and 10–30 pptv, addition of this third parameter results in a reverse of the curvature of the fit ($b$>1). It is likely that the intercept $c$ (equivalent to $5–6\times10^5$ molecule $cm^{-3}$) is higher than the true value of [OH] at night for these conditions, which during NAMBLEX, was measured below $6.09\times10^4$ molecule $cm^{-3}$. Hence the parameter $b$ is too high, being a mathematical consequence of the contributions to radical production at low $j-(O^1D$ from species which undergo photolysis at longer wavelengths than for $O^1D$ production from ozone. This unphysical situation appears to preclude the use of Eq. (10) to estimate nighttime OH levels from predominantly daytime OH data; rather, direct measurement at night is required.

An alternative to the empirical relationship between [OH] and $j-(O^1D)$ is to consider the relationship between [OH] and the rate of primary production of OH, P(OH) (defined in Eq. 1) during the campaign. If the formation of OH is dominated by ozone photolysis, and the OH removal rate is constant, reflecting constant chemical composition (usually with low $NO_x$ and VOC levels, where OH removal is dominated by reaction with CO and $CH_4$), a linear relationship between OH and P(OH) is expected (Eq. 4). Use of P(OH) rather than simply $j-(O^1D)$ incorporates variability in the primary production rate of OH due to changing ozone and water concentrations, and also temperature/pressure. Analysis of [OH] versus P(OH) for 22 days during the NAMBLEX campaign resulted in correlation coefficients ($r^2$) ranging from 0.13 (21 August, daily average NO=108.4 pptv) to 0.85 (9 August, daily average NO=18.0 pptv), with an average of 0.57 (campaign average NO=31.8 pptv).

**Table 2.** Results of fitting Eq. (10) to $OH/j-(O^1D)$ data sorted into NO bins i) NO=0–10 pptv, ii) NO=10–30 pptv, iii) NO=30–500 pptv.

| Fit | a | b | c | $r^2$ |
|---|---|---|---|---|
| i) | | | | |
| 1 Linear | 1.43±0.03 | 1 (fixed) | 0 (fixed) | 0.519 |
| 2 Power | 1.64±0.05 | 0.71±0.05 | 0 (fixed) | 0.593 |
| 3 Power/Intercept | 0.81±0.09 | 1.51±0.14 | 0.58±0.06 | 0.576 |
| ii) | | | | |
| 1 Linear | 1.68±0.02 | 1 (fixed) | 0 (fixed) | 0.462 |
| 2 Power | 1.90±0.03 | 0.68±0.03 | 0 (fixed) | 0.496 |
| 3 Power/Intercept | 1.11±0.09 | 1.22±0.09 | 0.64±0.07 | 0.515 |
| iii) | | | | |
| 1 Linear | 1.89±0.04 | 1 (fixed) | 0 (fixed) | 0.389 |
| 2 Power | 2.29±0.04 | 0.56±0.03 | 0 (fixed) | 0.509 |
| 3 Power/Intercept | 2.38±0.33 | 0.54±0.09 | −0.08±0.30 | 0.509 |

## 5.2 Steady state calculations of [OH]

### 5.2.1 Assuming production from ozone photolysis and loss by reaction with CO and $CH_4$ only

In the simplest case, considering only primary production ($O_3+h\nu\rightarrow O(^1D)+H_2O$) and loss through reaction with CO and $CH_4$, OH concentrations are given by Eq. (4), as outlined in Sect. 2. OH observations were compared with steady-state OH concentrations calculated from Eq. (4) for 200 s data averaging periods from 17 days of the campaign, the period limited by the co-availability of OH, CO and $CH_4$ data (Heard et al., 2005). The number of days on which steady state OH calculations were possible was increased to 21 by inferring CO and $CH_4$ levels from their correlations with acetylene and propane measurements (obtained by GC-FID; Lewis et al., 2005), as a strong correlation was observed between these species throughout the campaign (Heard et al., 2005). The CO/acetylene relationship was determined to be (CO/ppbv)=0.27($C_2H_2$/pptv)+68.88 ($r^2$=0.84), from the period 20 h prior to and 22 h subsequent to the gap in the CO data which ran from 04:28 GMT 17 August to 12:40 GMT 21 August. The same method was applied to calculate $CH_4$ from propane data for the interval from 04:27 GMT 17 August to 09:09 GMT 19 August, using the relationship ($CH_4$/ppbv)=0.85($C_3H_8$/pptv)+1754 ($r^2$=0.58).

Figure 5 compares the observed OH concentrations with the steady-state values calculated via Eq. (4), for two representative 48 h periods of the campaign. Figure 6 shows the hourly average calculated/observed OH ratio for 8 days (10, 15–21 August) which are used to compare [OH] calculations throughout Sect. 5.2 due to the co-availability of data for calculations using Eq. (12) (Sect. 5.2.2). Figure 6 displays a distinct diurnal profile in which OH is under-predicted early in the morning and in the late afternoon/early evening (high SZA) and over-predicted in the middle of the day. An

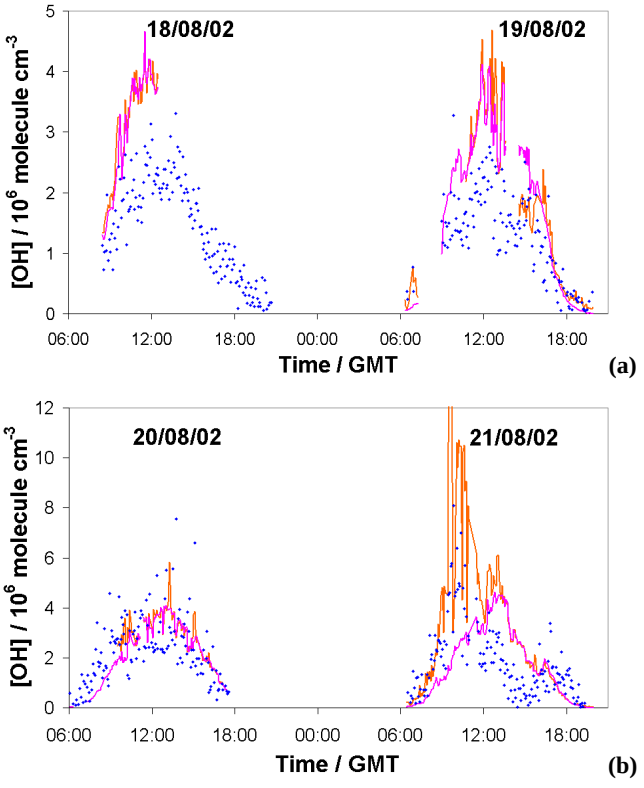


**Fig. 5.** Diurnal profiles of measured OH (blue diamonds), OH calculated using the simple steady state expression Eq. (4), which includes primary production from $O_3$ photolysis; and loss by reaction of CO and $CH_4$ only (pink line), and OH calculated by a more complex steady state expression (Eq. 11), which also includes $HO_2$+NO and $HO_2$+$O_3$ as OH sources, and also OH loss by reaction with *o*-VOCs (orange line) for representative 2-day periods: **(a)** 16–17 August **(b)** 20–21 August.

example of the early morning/late afternoon under-prediction of OH can be seen on 16 August (shown in Fig. 5a), when the calculated/observed OH ratio is less than 1 at the beginning and end of the diurnal. It is unlikely that over-prediction of OH sinks gives rise to the underprediction at high SZA, as Eq. (4) only includes loss of OH by reaction with CO and $CH_4$. Rather, this behaviour indicates the presence of additional OH sources at these times that are missing in the simple expression, for example recycling of $HO_2$ through reaction with $O_3$ and NO, and photolysis of HONO. OH may also be formed through the reaction of $O_3$ with alkenes, although this is unlikely to be significant under the relatively clean conditions encountered during NAMBLEX (Salisbury et al., 2001). Figure 6 also clearly demonstrates the general trend for the simple steady state Eq. (4) to over-predict [OH] between 09:00 and 17:00 GMT, where the campaign hourly average calculated/measured ratios varied between 1.00 and 1.69. At these times the majority of OH is formed from primary production which is included in Eq. (4), whereas there are OH sinks, in addition to CO and $CH_4$, which are not included in this expression.

#### 5.2.2 Adding other OH sources and sinks to the steady state expression for [OH]

The steady-state prediction of OH levels can be made more realistic through inclusion of additional OH sources and sinks. Equation (4) was extended to include OH production through reaction of $HO_2$ with NO and with $O_3$, and OH loss through reaction with *o*-VOCs methanol, acetaldehyde and acetone. These species were selected for inclusion on the basis of Rate of Production Analyses (ROPAs) carried out using the MCM (Sommariva et al., 2005) and by simple kinetic calculations using measured hydrocarbons and *o*-VOCs (Lewis et al., 2005). The ROPAs identified the three main sources of OH, on average, as $HO_2$+NO (41%), $O^1D$+$H_2O$ (31%) and $HO_2$+$O_3$ (24%). Calculation of the mean pseudo-first-order loss rates for OH due to reactions with various species showed that on average, CO (44%), $CH_4$ (16%) and *o*-VOCs (including only acetaldehyde, methanol and acetone) (17%) were the major sinks during NAMBLEX, with non-methane hydrocarbons being less important (Read et al., 2003; Lewis et al., 2005). The OH steady-state expression was extended to incorporate these species, resulting in Eq. (11), given below:

$$[\mathrm{OH}]_{ss} = \frac{\mathrm{P(OH)} + X}{k'} \quad (11)$$

where

$$X = (k_{\mathrm{HO_2+O_3}}[\mathrm{O_3}] + k_{\mathrm{HO_2+NO}}[\mathrm{NO}])[\mathrm{HO_2}],$$

and

$$k' = k_{\mathrm{OH+CO}}[\mathrm{CO}] + k_{\mathrm{OH+CH_4}}[\mathrm{CH_4}] + \sum k_{\mathrm{OH}+o\mathrm{VOCs}}[o\mathrm{VOCs}]$$

The *o*-VOCs included are acetaldehyde, methanol and acetone.

The co-availability of data limited the use of Eq. (11) to 10 days of the campaign, between 10 August and 1 September. Plots of the results of these calculations for the periods 16–17 and 20–21 August are shown in Fig. 5. The hourly averaged calculated/measured [OH] ratios for the 8 comparison days are shown in Fig. 6. Figure 5 shows that inclusion of additional reactions has made little difference to the calculated/measured [OH] ratios on 17 and 20 August, indicating that the additional sources and sinks are small on these days. However, there are notable differences between [OH] calculated using Eqs. (4) and (11) for 16 and 21 August. Considering the campaign averaged calculated/measured [OH] ratio shown in Fig. 6, the additional OH production terms have resulted in better agreement in the early morning and late afternoon/evening; although there still appears to be a source(s) missing at these times. The photolysis of HONO is a candidate, but as HONO was not measured during NAMBLEX, it is difficult to speculate on this.

On 16 August between 10:00 and 14:00 GMT, the average calculated/measured [OH] ratio increases from an average of

**Table 3.** The range, mean and 1$\sigma$ standard deviations in the calculated/measured [OH] ratios for calculations carried out with Eq. (4), Eq. (11) with various modifications to include loss of OH to $NO_2$ and both $NO_2$ and HCHO and Eq. (12). All the data shown are from calculated from 522 data points (200 s average) on 8 days (10 and 15–21 August).

| | Lower | Upper | Mean | St Dev |
|---|---|---|---|---|
| Eq. (4) | 0.01 | 11.07 | 1.24 | 0.62 |
| Eq. (11) | 0.12 | 10.90 | 1.38 | 0.45 |
| Eq. (11) inc OH+$NO_2$ | 0.11 | 10.83 | 1.34 | 0.46 |
| Eq. (11) inc OH+$NO_2$ and OH+HCHO | 0.11 | 9.55 | 1.24 | 0.39 |
| Eq. (12) | 0.09 | 7.93 | 0.94 | 0.39 |
| Eq. (12) excluding isoprene and DMS | 0.10 | 8.68 | 1.13 | 0.36 |

1.10 for calculations made using Eq. (4) to 1.85 for calculations made using Eq. (11), attributed mainly to the addition of the $HO_2$+NO reaction, which increases the calculated [OH] (NO levels are high – up to 355 pptv). Including the reaction OH+$NO_2$ ($NO_2$ levels are up to 690 pptv) as a loss for OH only has a small effect (OH is still over-predicted by an average factor of 1.79 between 10:00–14:00 GMT), suggesting other sinks need to be included during this polluted period. For 21 August, the shape of the OH profile is calculated more accurately, with a peak in [OH] predicted just before 10:00 GMT when NO, and hence the rate of OH production from the $HO_2$+NO reaction, is at a maximum. The inclusion of production of OH through $HO_2$+$O_3$ and $HO_2$+NO, and loss of OH through reaction with the *o*-VOCs, has mixed results for the steady-state calculation of [OH].

Figure 6 illustrates that the net effect of the additional source and sinks increases [OH] and hence improves the calculated/measured ratio at the beginning (before 09:00 GMT) and end (after 18:00 GMT) of the day. However, in the middle of the day (between 09:00 and 18:00 GMT), the net effect of additional sources and sinks has worsened the model/measured [OH] ratio, and hence the average model/measured [OH] ratio (for the 8 comparison days) has increased from 1.24±0.62 to 1.38±0.45 for Eqs. (4) and (11), respectively. Addition of the OH+$NO_2$ reaction (Fig. 6) improves the agreement by only ∼4%, but addition of OH+HCHO leads to a significant improvement (1.24±0.39). See Table 3 for a summary of the results of all steady state [OH] calculations.

As mentioned above, non-methane hydrocarbons (NMHC) are not yet included as sinks for OH. Using the campaign averaged concentration of NMHC species measured during NAMBLEX (Lewis et al., 2005, this issue), with kinetic data taken from Sander et al. (2003) and Atkinson et al. (2002), an average loss rate for OH by reaction with all other hydrocarbons was calculated to be $k'_{HC,\mathrm{tot}}$=0.17 $\mathrm{s}^{-1}$ and was included as an OH sink, together with $NO_2$ and HCHO. Dimethyl sulphide (DMS) and isoprene, which are both highly reactive towards OH, are included in this calculation. Their concentrations displayed a very high variability during the campaign on account of their specific localised sources (Lewis et al., 2005; Heard et al., 2005), and if they are not included as OH sinks $k'_{HC,\mathrm{tot}}$ drops to 0.085 $\mathrm{s}^{-1}$. Inclusion of the additional sinks results in a modified steady-state expression:

$$[\mathrm{OH}]_{ss} = \frac{\mathrm{P(OH)} + X}{k'} \quad (12)$$

where,

$$X = (k_{\mathrm{HO_2+O_3}}[\mathrm{O_3}] + k_{\mathrm{HO_2+NO}}[\mathrm{NO}])[\mathrm{HO_2}]$$

and

$$k' = k_{\mathrm{OH+CO}}[\mathrm{CO}] + k_{\mathrm{OH+CH_4}}[\mathrm{CH_4}] + \sum k_{\mathrm{OH}+o\mathrm{VOCs}}[o\mathrm{VOCs}] + k_{\mathrm{OH+NO_2}}[\mathrm{NO_2}] + k_{\mathrm{OH+HCHO}}[\mathrm{HCHO}] + k'_{HC,\,\mathrm{tot}}$$

The results of calculations of [OH] carried out using Eq. (12) are shown in Fig. 6. Inclusion of $k'_{HC,\mathrm{tot}}$ resulted in a further 16% reduction in the calculated/measured [OH] on average, now being 0.94±0.39 for the 8 days (522 data points, 200 s average) for which all measurements were available. If DMS and isoprene are not included, this average ratio is 1.13±0.36. Figure 6 also shows that calculations of [OH] carried out using Eq. (12) are closest in both magnitude and profile shape to measured [OH]. A summary of the results of all [OH] steady state calculations can be found in Table 3.

In Sommariva et al. (2005) of this issue, [OH] is calculated using a box model incorporating the MCM that is constrained by the full suite of measured OH sources and sinks, including halogen species. The period for which OH can be calculated by the full MCM is more limited (availability of data), and the average model/measured [OH] is 1.07±0.64. For the equivalent period the corresponding ratios using Eqs. (4) and (12) are 1.17±0.69 and 1.12±0.53, being within 10 and 5% of the MCM model, respectively. Although the simple expressions perform well, on average, additional OH sources and sinks can sometimes balance one another out, and close agreement with the measured OH may not imply a thorough understanding of the processes controlling the chemistry of

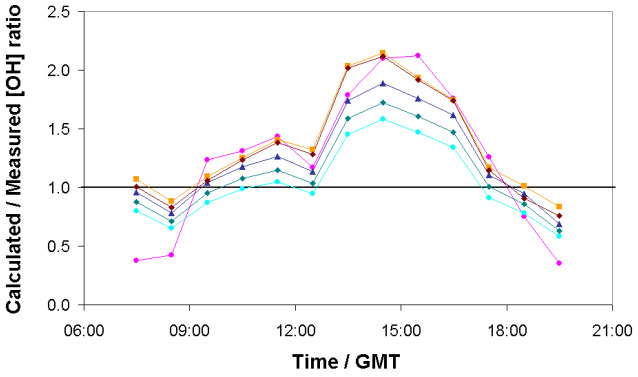


**Fig. 6.** Campaign averaged diurnal of the hourly average calculated/measured [OH] ratio for Eq. (4) (pink circles), Eq. (11) (orange squares), Eq. (11) including loss of OH to $NO_2$ (brown diamonds), Eq. (11) including loss of OH to $NO_2$ and HCHO (navy blue triangles), Eq. (12) which includes all of the above and also reaction with non-methane hydrocarbons (light blue circles), and Eq. (12) but excluding isoprene and DMS (green diamonds). The graph is constructed from 522×200 s averaged data points taken on 8 days between 10 and 21 August when all co-reactant data were available. Uncertainties are omitted for clarity. The mean calculated/measured OH ratios for all calculations are summarised in Table 3.

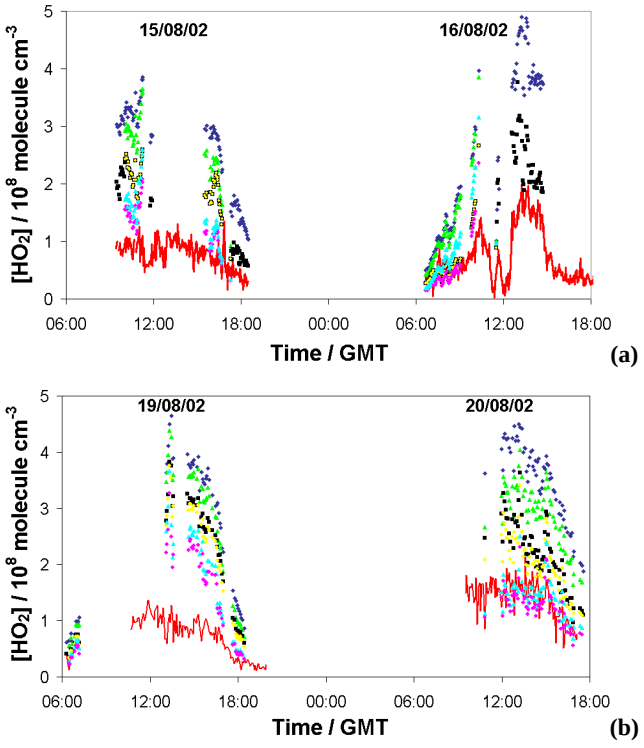


**Fig. 7.** Diurnal profiles of measured $HO_2$ (red line), and steady-state calculated $HO_2$ derived using Eq. (5) (navy blue diamonds) and several modifications which also include: loss by reaction of $HO_2$ with measured IO (green triangles), loss by reaction of $HO_2$ with measured IO×10 (light blue triangles), uptake of $HO_2$ onto aerosol (black squares), both loss of $HO_2$ by reaction with IO and by uptake onto aerosol (yellow circles with or without black border) and both loss of $HO_2$ by reaction with IO×10 and uptake onto aerosols (pink circles). The data shown are from **(a)** 15–16 August **(b)** and 19–20 August. It was not possible to calculate $HO_2$ between 11:57 and 15:26 GMT on the 15 August as $O_3$ data adjacent to the FAGE instrument were not available.

OH, and a full mechanism is necessary. Several groups are now directly measuring the total reactivity of OH, $k'$, through its total loss rate in the field, which provides an additional constraint for comparison with models.

### 5.3 Steady state calculations of $HO_2$

#### 5.3.1 Solution of the cubic Eq. (5) for the "mini" mechanism

Steady-state $HO_2$ concentrations can be calculated using the cubic expression (5) (Sect. 2) developed by Carslaw et al. (1999b). In this section we compare observed [$HO_2$] with those calculated using Eq. (5), and a modified form incorporating the reactions of $HO_2$ with halogen monoxide species and also loss to aerosol, which have been advanced previously as possible explanations for model overpredictions of $HO_2$ measurements made in the MBL (Kanaya et al., 2002; Sommariva et al., 2004; Haggerstone et al., 2005). Steady state $HO_2$ calculations were possible on 9 days of the campaign, maximised by using CO-acetylene and $CH_4$-propane correlations to fill gaps in CO and $CH_4$ data. There were also two short intervals for which $H_2$ measurements were not available, the first from 06:38 GMT 10 August to 15:56 GMT 13 August, and the second from 05:48 GMT 17 August to 14:39 GMT 21 August, for which $H_2$ levels were interpolated from adjacent measurements. This method for inferring $H_2$ levels was considered to be viable as the variation in the mixing ratio of $H_2$ was small throughout the NAMBLEX campaign (overall range of 460–610 ppbv) and also the OH+$H_2$ reaction was found to only make a small contribution of 4.2% to $HO_2$ production. Equation (5) was solved iteratively following computation of the parameters (see Appendix A) from measured co-reactant concentrations (CO, $H_2$, HCHO, $CH_4$, $NO_2$, NO, $O_3$, $P$(OH) and $j-$(HCHO)) and literature rate coefficients. The results of the [$HO_2$] calculations from four representative days of the campaign (15–16 and 19–20 August) are displayed in Fig. 7, and the hourly averaged calculated/measured $HO_2$ ratios for 6 days (13, 15–16, 18–20 August) which are used for comparison of calculated [$HO_2$] throughout Sect. 5.3 are shown as a function of time-of-day in Fig. 8.

Figure 7 illustrates that Eq. (5) (no halogen chemistry or aerosol loss included) significantly overestimates the observed $HO_2$. Over the 9 days for which calculations of [$HO_2$] were possible the cubic expression over-predicted $HO_2$ by an average factor of 4.2±1.6 (1$\sigma$). Using co-measurements of IO and BrO made during the NAMBLEX

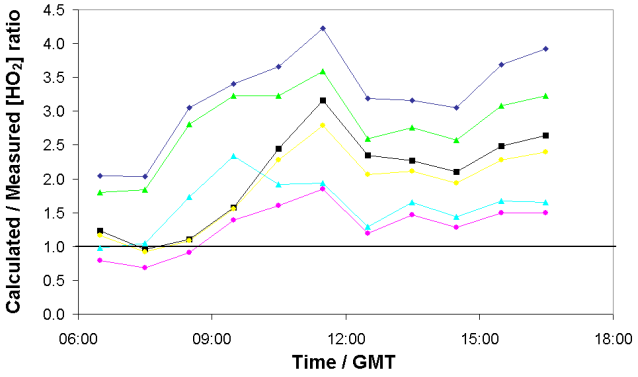


**Fig. 8.** Campaign average of the hourly averaged calculated/measured [$HO_2$] ratio using Eq. (5) (navy blue diamonds) and several modifications which also include: loss by reaction of $HO_2$ with measured IO (green triangles), loss by reaction of $HO_2$ with measured IO×10 (light blue triangles), uptake of $HO_2$ onto aerosol (black squares), both loss of $HO_2$ by reaction with IO and by uptake onto aerosol (yellow circles) and both loss of $HO_2$ by reaction with IO×10 and uptake onto aerosol (pink circles). The graph is constructed from 281×200 s averaged data points on 6 days (13, 15–16, 19–20 August) when all co-reactant data were available. Uncertainties are omitted for clarity. The mean calculated/measured $HO_2$ ratios for all calculations can be found in Table 4.

campaign, Bloss et al. (2005a) and Sommariva et al. (2005) have investigated the impact of halogen monoxides on the concentrations of OH and $HO_2$ through the following reactions:

$$HO_2 + XO \rightarrow HOX + O_2 \quad \text{(R5)}$$

$$HOX + h\nu \rightarrow OH + X \quad \text{(R6)}$$

$$HOX + \text{aerosol} \rightarrow \text{loss} \quad \text{(R7)}$$

Sommariva et al. (2004) and Haggerstone et al. (2005) have examined the impact upon $HO_x$ budgets from the heterogeneous uptake of $HO_2$ onto aerosols, concluding that the uptake of $HO_2$ onto sea-salt particles plays a crucial role. During NAMBLEX, IO, BrO, aerosol number density and size distribution were measured together with OH and $HO_2$ for the first time in the MBL, permitting a more quantitative evaluation of OH and $HO_2$ budgets.

### 5.3.2 Impact of halogen monoxides

IO and BrO were measured using long-path Differential Optical Absorption Spectroscopy (DOAS), as described by Saiz-Lopez et al. (2004a, b, 2005, 2006). Briefly, the analysis light path was directed from Mace Head to Croaghnakeela Island, 4.2 km offshore to the West of Mace Head, and back via a retro reflector to the receiving telescope and optics, giving a total beam path of 8.4 km, approximately 10 m above sea level. Seven days with 69 hourly averaged IO data

**Table 4.** The range, mean and 1$\sigma$ standard deviations in the calculated/measured [$HO_2$] ratios for calculations using Eq. (5) with various modifications to include loss of $HO_2$ to: IO, IO×10, uptake onto aerosol ($\gamma_{HO_2}$=1.0), IO + uptake onto aerosol ($\gamma_{HO_2}$=1.0) and IO×10 + uptake onto aerosol ($\gamma_{HO_2}$=1.0). All the data shown are calculated from 281 data points (200 s average) on 6 days (13, 15–16 and 18–20 August).

| | Lower | Upper | Mean | St Dev |
|---|---|---|---|---|
| Eq. (5) | 1.16 | 6.93 | 3.22 | 0.69 |
| Eq. (5) + IO | 1.00 | 6.17 | 2.79 | 0.57 |
| Eq. (5) + (IO×10) | 0.46 | 4.68 | 1.60 | 0.39 |
| Eq. (5) + aerosols | 0.47 | 5.27 | 2.03 | 0.71 |
| Eq. (5) + IO + aerosols | 0.46 | 4.9 | 1.87 | 0.61 |
| Eq. (5) + IO×10 + aerosols | 0.35 | 4.74 | 1.29 | 0.36 |

points could be matched to the 200 s averaged $HO_2$ measurements. The loss of $HO_2$ by reaction with IO was included in the steady-state analysis by adding $k_{HO_2+IO}$ (using $k_{HO_2+IO}=1.4\times10^{-11}\exp^{554/T}$; Knight and Crowley, 2001) to the loss term (B) for calculating $\beta, \gamma, \delta$ and $\varepsilon$ (see Appendix A and Carslaw et al., 1999b, for a full description of the expression and all of its terms). Solution of this modified Eq. (5) results in steady state $HO_2$ concentrations which reflect the maximum possible effect of the $HO_2$+IO reaction, as photolysis of the resultant HOI to produce OH, which can then be recycled to $HO_2$ by reaction with CO and $O_3$, is not considered. The revised steady-state $HO_2$ concentrations are shown in Figs. 7 and 8, with inclusion of $HO_2$+IO significantly reducing the calculated/measured [$HO_2$] ratio whilst still retaining the shape of the $HO_2$ diurnal profile. Reductions in the calculated/measured $HO_2$ ratio compared to the original calculation from Eq. (5) range from 0.5 to 39.1%, with an average of 14±5% (1$\sigma$). Despite the significant reduction, there is still a general over-prediction of $HO_2$, with calculated to measured ratios ranging between 1.0–6.2 with an average of 2.8±0.6 (see Table 4 for a summary of these results).

The above analysis uses IO concentrations averaged over the DOAS beampath. If the principal iodine sources at Mace Head are dominated by local, coastal seaweed emissions of alkyl iodides and molecular iodine, rather than being open ocean in origin, then the IO concentrations at Mace Head may be significantly higher than the beampath average, while those over the open-ocean portion are correspondingly lower. Saiz-Lopez et al. (2006), provide compelling evidence that the iodine activity is concentrated in a 400 m wide zone next to the shoreline, indicating that the local, Mace Head IO concentrations are likely to be up to a factor of 10 higher than those returned by the DOAS system. Adding IO concentrations at a level of 10× that measured by DOAS (10×IO) to Eq. (5) resulted in the calculated/measured ratio being decreased by an average of a further 45±7% (1$\sigma$),

with a calculated/measured $HO_2$ ratio of between 0.5 and 4.7 and an average of 1.6±0.4 (see Figs. 7 and 8). Thus by including loss of $HO_2$ by reaction with IO at levels a factor of 10 higher than the DOAS measurements there is a significant improvement in the average calculated/measured $HO_2$ ratio, although for some time points the increased IO causes the steady state calculations to underpredict $HO_2$ by as much as 50%. This may arise as a consequence of the omission of the buffering of the additional $HO_2$ loss through photolysis of HOI, and recycling of the resultant OH to $HO_2$ via reaction with $O_3$ and CO. In addition, $HO_2$ may not be in photochemical equilibrium if the $HO_2$ lifetime (1–2 min) is comparable with the transport time of the sampled air over the relatively narrow iodine emission region prior to reaching the FAGE instrument. Box model simulations of the impact of IO upon $HO_2$ during NAMBLEX (Sommariva et al., 2005), found that using 10×IO resulted in good agreement with the measurements on most days.

The conversion of $HO_2$ to HOI results in an additional source of OH from HOI photolysis. The OH steady state Eq. (11) was modified to include an additional OH production term, accounting for HOI photolysis:

$$\text{Rate of production of OH from HOI photolysis} = (k_{HO_2+IO}[HO_2][IO])\frac{j-(\text{HOI})}{j-(\text{HOI})k'} \quad (13)$$

where $j-$(HOI) is the rate of photolysis of HOI and $k'$ is the pseudo-first-order rate coefficent for loss of HOI to aerosol, using an HOI uptake coefficient of 0.6 (Sommariva et al., 2005). Including OH production from HOI photolysis increases [OH], averaged over 24 h, by 39%, very similar to the results of Bloss et al. (2005a) and when HOI photolysis is included in the full model (Sommariva et al., 2005). The effect on $[OH]_{ss}$ is dependent on the time of day, being considerably larger early and late in the day, when photolysis of $j-$(HOI) is relatively more important as an OH source as values of $j-(O^1D)$, and hence P(OH), are reduced. During the middle of the day, 09:00–16:59 GMT, the effect on $[OH]_{ss}$ is on average 23% (20% at noon itself).

The reaction of BrO with $HO_2$ has the potential to reduce the calculated $HO_2$ in a qualitatively similar way to IO. DOAS measurements of BrO were made on 6 days of the NAMBLEX campaign, with a maximum daytime concentration of 6.6 pptv seen on 4 August. (Saiz-Lopez et al., 2004b). Matching of the 63 hourly averaged BrO data points to the 200 s $HO_2$ data allowed $HO_2$ to be calculated using Eq. (5), modified to include the $HO_2$+BrO with $k_{HO_2+BrO}$ (Bloss et al., 2002; Sander et al., 2003), although $HO_2$ measurements were only made on one of these, namely 10 August. On this day the calculated/measured $HO_2$ ratio was seen to decrease by between 1.8 and 10.5% with an average reduction of 6.2% compared to the original calculations of $[HO_2]$ carried out using Eq. (5) (excluding BrO). Again, these calculations only demonstrate the maximum possible effect of loss of $HO_2$ via reaction with BrO, as we have assumed that all HOBr is lost onto aerosols and that none is photolysed. This assumption is more valid in the case of HOBr than for HOI, as the rate of photolysis of HOBr is a factor of 4.5 lower than that for HOI. The lower rate of photolysis of HOBr results in a reduced buffering of the $HO_2$ loss through the recycling of the resultant OH (by reaction with $O_3$ and CO) compared to that seen through photolysis of HOI.

#### 5.3.3 Impact of $HO_2$ uptake to aerosol

Another possible cause for over-prediction of the observed $HO_2$ levels is the omission of the uptake of $HO_2$ onto aerosol. The lifetime of $HO_2$ in the clean MBL air is of the order of 1–2 min, and so the heterogeneous uptake of $HO_2$ onto aerosols has the potential to significantly influence the $HO_x$ budget. During NAMBLEX, detailed measurements of the size-dependent chemical and physical properties of particles were made (Coe et al., 2005) and these data were used to calculate pseudo-first-order rate coefficients for the uptake of $HO_2$ onto aerosol particles (Sander, 1999; Haggerstone et al., 2005; Sommariva et al., 2005; Bloss et al, 2005a). $HO_2$ aerosol uptake rates ($k'_{aerosol}$) were derived from ambient humidity aerosol size distributions (from 3 nm to 30 microns, assembled from a combination of mobility, backscatter and forward scattering measurements) considering mass transfer in the transition regime, and using a reaction probability of $\gamma_{HO_2}$=1.0 (theoretical maximum). There is a large variation in the available literature values for the $HO_2$ uptake coefficient upon wet sea-salt aerosol (Thornton and Abbatt, 2005), leading to a large source of uncertainty in the calculated rate of $HO_2$ uptake and hence we use $\gamma_{HO_2}$=1.0 to investigate the maximum possible impact of heterogeneous chemistry upon $HO_2$ concentrations. The $HO_2$ loss term used to calculate $\beta$, $\gamma$, $\delta$, and $\varepsilon$ (see Appendix A) was modified using 1475 $k'_{aerosol}$ data points calculated on a 30 min time basis and matched to the 200 s $HO_2$ measurements.

The effect of including aerosol uptake is shown on Figs. 7 and 8. There is a significant reduction in the calculated/measured $HO_2$ ratio, ranging from 12 to 72% with an average reduction of 38±12% ($1\sigma$) compared to the original calculations using Eq. (5). Similar to the results found for addition of the $HO_2$+IO reaction to Eq. (5), it is clear that uptake of $HO_2$ onto aerosols alone cannot account for the over-prediction of $HO_2$, with an overall mean $HO_2$ calculated/measured ratio of 2.0±0.7 ($1\sigma$). The exception occurs on the morning of 16 August when the addition of uptake of $HO_2$ onto aerosols to Eq. (5) results in an average calculated/measured $HO_2$ ratio of 1.0±0.3 ($1\sigma$) between 06:40 and 09:03 GMT. The addition of uptake of $HO_2$ onto aerosols generally causes a greater reduction in the calculated/measured $[HO_2]$ ratio than that seen on addition of the $HO_2$+IO reaction, the exception to this being on 18 August when the campaign maximum IO were measured (up to 5 pptv). Inclusion of the uptake of $HO_2$ onto aerosols in Eq. (5) causes an average of an additional 23% reduction in

the calculated/measured [$HO_2$] ratio compared to that found on inclusion of $HO_2$+IO. Uptake of $HO_2$ onto aerosols appears to play an important role in the free-radical chemistry of the MBL, but further studies of the physical and chemical properties of aerosols and, in particular, the rate coefficients for the heterogeneous uptake of $HO_2$ radicals onto realistic aerosol surfaces are required to further our understanding of the $HO_x$ cycle in this environment.

#### 5.3.4 Combined effect of halogen oxides and aerosol uptake upon $HO_2$

In the two preceding subsections it was shown that the reaction of $HO_2$ with IO or the uptake of $HO_2$ onto aerosols cannot in isolation account for the over-prediction of $HO_2$ when using Eq. (5). Hence, in an attempt to more accurately predict $HO_2$, both loss mechanisms were included in Eq. (5), and $HO_2$ was recalculated in the manner described above. This allowed calculations of $HO_2$ to be made on 6 days of the campaign, several examples of which are shown in Fig. 7, with the hourly average calculated/measured [$HO_2$] ratios for the 6 comparable days in Fig. 8. Addition of both loss of $HO_2$ via reaction with IO (using DOAS measured values) and uptake onto aerosols resulted in reductions in the calculated/measured $HO_2$ ratio of between 13 and 72%, with an average reduction of 43±10% (1$\sigma$) compared to the original calculations carried out using Eq. (5). However, even with the cumulative effects of the addition of both loss of $HO_2$ via reaction with IO and uptake onto aerosols the modified Eq. (5) still over-predicts the observed $HO_2$ by a factor of 1.9±0.6 (1$\sigma$). It is only on addition of both IO×10 and uptake of $HO_2$ onto aerosols that agreement (within uncertainty) between the calculated and measured $HO_2$ concentrations is achieved, with an average calculated/measured ratio of 1.3±0.4 (1$\sigma$).

In order to consider the additional reduction in the calculated $HO_2$ levels due to reaction with BrO in addition to reaction with IO and heterogeneous uptake, it was necessary to determine typical BrO levels (simultaneous DOAS measurements of IO and BrO were not possible due to the different spectral ranges of their principal absorption features). Hourly averages of BrO between 10:00 and 14:00 GMT were determined over the whole campaign, and were used along with the hourly averages of all other necessary parameters for the 6 comparable days in order to calculate new values for $\beta$, $\gamma$, $\delta$, and $\varepsilon$ such that loss of $HO_2$ via reaction with IO, BrO and uptake onto aerosols were included in Eq. (5). Using these typical BrO levels it was found that inclusion of the reaction of $HO_2$+BrO only reduced the calculated/measured [$HO_2$] ratio by a further 3.1±1.0% (1$\sigma$) on average. The results of calculations of $HO_2$ using Eq. (5) with various loss schemes are summarised in Table 4.

In Sommariva et al. (2005) of this issue a box model using the MCM was used to calculate [$HO_2$]. Using a scheme which does not include halogens/aerosol uptake the modelled/measured $HO_2$ ratio is 2.43±0.82, averaged between 15 and 20 August, which improves to 1.09±0.42 if uptake to aerosol ($\gamma_{HO_2}$=1.0) and the reaction $HO_2$+IO is included. Further to this Sommariva et al. (2005) find that if the hypothesis that the IO concentrations at the $HO_2$ measurements site are a factor of 10 greater than those measured as the average across the DOAS light-path (Saiz-Lopez et al., 2005), then $\gamma_{HO_2}$ is likely to be significantly smaller than 1.0 (consistent with the findings of Thornton and Abbat, 2005) as otherwise $HO_2$ would be significantly underpredicted by the model.

## 6 Discussion

### 6.1 $HO_x$ observations

Concentrations of OH measured during NAMBLEX are in good agreement with those measured previously at Mace Head (Creasey et al., 1997, 2002; Berresheim et al., 2002), although significantly lower than the levels observed by Berresheim et al. (2003) at a coastal site in Crete during the MINOS campaign, where levels of $NO_x$ were considerably higher. There was a good correlation between [OH] and $j(O^1D)$ (Figs. 2 and 4), but not as good as observed during MINOS or SOAPEX-2 (Cape Grim, Creasey et al., 2003), because of more short-term variability in the OH concentrations, probably due to more local variability in co-reactant concentrations at the Mace Head site. The 24 h average OH concentration, $9.1\times10^5$ molecule cm$^{-3}$, agrees well with estimates for the northern hemisphere troposphere derived from methyl chloroform data (e.g. Prinn et al., 2001; mean OH=$(8.98\pm2.02)\times10^5$ molecule cm$^{-3}$).

The daytime $HO_2$ levels were also comparable with those measured previously at Mace Head (e.g. Creasey et al., 2002). Measurements of total [$RO_2$] by the PERCA (PEroxy Radical Chemical Amplifier) technique during NAMBLEX indicated that $HO_2$ comprised between 20 and 40% of the total $RO_2$ radicals during the daytime, falling to ca. 15% overnight. The $RO_2$ radical measurements, and specifically the $HO_2$/total $RO_2$ ratio, are described in more detail in Fleming et al. (2005).

### 6.2 OH steady-state analysis

The gross features of the dataset of OH concentrations could be replicated using a very simple steady-state expression incorporating only primary production from ozone photolysis and loss by reaction with $CH_4$ and CO. Including the reactions of $HO_2$ with NO and $O_3$ as an OH source and the reactions of OH with *o*-VOCs, HCHO, $NO_2$ and non-methane hydrocarbons improved the agreement, with an average calculated to measured OH concentration of 0.94±0.39 (1.13±0.36 if isoprene and DMS are not included). This ratio is consistent with the value of 1.07±0.64 obtained using the box model employing the MCM (Sommariva et al.,

2005), and also with the predictions of a global chemistry-transport model (GEOS-CHEM), which overestimated the observed OH by 25% for the NAMBLEX campaign (Bloss et al., 2005b). Despite the average ratio being close to unity, examination of Fig. 6 clearly shows that the calculated to modelled OH ratio displays a considerable diurnal variation, with steady-state calculations underestimating OH in the early morning and evenings, and overestimating OH during the middle of the day. The overestimation is not too surprising as not all OH sinks are included in the steady-state expression. The underprediction at higher SZA suggests that other sources are missing in the analysis, for example photolysis of suitable precursors at longer wavelengths than required for $O_3$ photolysis. The reaction of $O_3$ with alkenes is not a significant source of daytime $HO_x$ under the relatively clean conditions experienced during NAMBLEX (Sommariva et al., 2005). HONO was not measured, and so the net result of HONO photolysis to give OH and its formation from the OH+NO+M reaction has not been evaluated but under the predominantly low $NO_x$ environment of Mace Head is not expected to be significant source of OH (Carslaw et al., 2002).

### 6.3 $HO_2$ steady-state analysis

Using $HO_2$ data from the NAMBLEX campaign we have been able to test the ability of a cubic expression, Eq. (5), derived using a reduced mechanism of an MCM model tailored to conditions at Mace Head (Carslaw et al., 1999b), to predict $HO_2$. The calculations are able to capture the general features of the $HO_2$ diurnal profiles, but fail to accurately predict the absolute concentration of $HO_2$, with a mean calculated to observed [$HO_2$] ratio of 3.22±0.69. Addition of $HO_2$ sinks in the form of reaction with IO and uptake onto aerosols reduces this value to 1.87±0.61 for the 6 days over which co-reactant data were available. Including loss of $HO_2$ by reaction with 10 times the IO measured by DOAS, accounting for the non-uniform distribution of iodine species thought to be present along the DOAS beampath at Mace Head (Saiz-Lopez et al., 2006), together with uptake of $HO_2$ onto aerosols, gave a further agreement to give a ratio of 1.29±0.36. The analysis does not include buffering of the loss of $HO_2$ through photolysis of HOI (formed by $HO_2$+IO) and recycling of the resultant OH through reaction with $O_3$ and CO back to $HO_2$. In this manner OH could be increased on average by 43% in the early morning/late afternoon and on average by 23% in the middle of the day. Also, the fetch over the shoreline region which acts as the major iodine source is of the order of 400 m and transport times over this region may be comparable to the lifetime of $HO_2$ (1–2 min), and thus $HO_2$ may not be in photochemical steady state, as is assumed in the derivation of Eq. (5).

## 7 Conclusions

OH and $HO_2$ radicals have been measured at the Mace Head Atmospheric Research Station during July and August 2002 by laser induced fluorescence. OH was measured on 24 days and showed a distinct diurnal profile, strongly correlated with $j-(O^1D)$, with maximum OH concentrations observed at noon of $(3–8)\times10^6$ molecule $cm^{-3}$. $HO_2$ was observed on 17 days, with maximum mixing ratios in the range 3.5–8 pptv. A simple steady-state expression was used to calculate OH which included loss by reaction with CO, $CH_4$, HCHO, $NO_2$, methanol, acetaldehyde, acetone and an average total loss by reaction with non-methane hydrocarbons, and production by $O_3$ photolysis and the reactions of $HO_2$ with NO and $O_3$. An average ratio of OH calculated using this expression to measured OH was 0.94±0.39. Inclusion of the oxygenated species, which had not previously been measured at Mace Head, improved the agreement considerably. Although the average ratio is close to unity, the ratio displayed a distinct diurnal variation, with the model overpredicting in the middle of the day and underpredicting in the early morning and late afternoon/evening. $HO_2$ concentrations were calculated using a cubic equation which is an analytic solution to a simple chemical mechanism previously developed for the remote MBL. The calculation overestimates $HO_2$, but the agreement with measurement is improved considerably by the inclusion of heterogeneous loss of $HO_2$ to aerosol, and reaction of $HO_2$ with the halogen oxides IO and BrO giving a calculated/measured [$HO_2$] ratio of 1.29±0.36.

## Appendix A

As discussed in Carslaw et al. (1999b, 2002), a reduced "mini" mechanism, consisting of 25 reactions and 17 species, leads to the following cubic equation for the concentration of $HO_2$:

$$\beta[HO_2]^3 + \gamma[HO_2]^2 + \delta[HO_2] + \varepsilon = 0 \quad \text{(A1)}$$

where,

$$\beta = 2k_{T2}(k_{T3}B + k_{T1}A) \quad \text{(A2)}$$

$$\gamma = 2k_{T3}k_{T2}J_1 + 2k_{T3}k_{p5}[NO]B + 2k_{T2}k_{p4}[CH_4]B + k_T[NO_2]k_{T2}B + 2Ak_{T1}k_{p5}[NO] \quad \text{(A3)}$$

$$\delta = 2k_{T3}k_{p5}J_1[NO] + 2k_{T2}k_{p4}J_1[CH_4] + k_TJ_1[NO_2]k_{T2} + k_TB[NO_2]k_{p5}[NO] - (J_1 + J_2)Ak_{T2} \quad \text{(A4)}$$

$$\varepsilon = J_1k_T[NO_2]k_{p5}[NO] - (J_1 + J_2)Ak_{p5}[NO] \quad \text{(A5)}$$

where,

$$J_1 = P(OH) = 2f[O_3]j - (O^1D) \quad \text{(A6)}$$

$$J_2 = 2j - (HCHO \rightarrow 2HO_2)[HCHO] \quad \text{(A7)}$$

$$A = k_{CO+OH}[CO] + k_{H_2+OH}[H_2] + k_{HCHO+OH}[HCHO] + k_{CH_4+OH}[CH_4] + k_{NO_2+OH}[NO_2] + k_{O_3+OH}[O_3] \quad \text{(A8)}$$

$$B = k_{HO_2+NO}[NO] + k_{HO_2+O_3}[O_3] \quad \text{(A9)}$$

$$k_T = k_{OH+NO2} \quad \text{(A10)}$$

$$k_{T1} = k_{HO_2+HO_2} \quad \text{(A11)}$$

$$k_{T2} = k_{HO_2+CH_3O_2} \quad \text{(A12)}$$

$$k_{T3} = k_{OH+HO_2} \quad \text{(A13)}$$

$$k_{p4} = k_{CH_4+OH} \quad \text{(A14)}$$

$$k_{p5} = k_{CH_3O_2+NO} \quad \text{(A15)}$$

*Acknowledgements.* Thanks are given to K. Read for assistance with the preparation of this manuscript. We are also grateful to the other participants of NAMBLEX for providing data used in the analysis and interpretation of OH and $HO_2$ measurements. We are grateful to the NERC for funding this work under grant number NER/A/S/2000/01313.

Edited by: P. Monks

## References

Atkinson, R., Baulch, D. L., Cox, R. A., Crowley, J. N., Hampson, R. F., Kerr, J. A., Rossi, M., and Troe, J.: Summary of evaluated kinetic and photochemical data for atmospheric chemistry, see http://www.iupac-kinetic.ch.cam.ac.uk/, 2002.

Berresheim, H., Elste, T., Tremmel, H. G., Allen, A. G., Hansson, H. C., Rosman, K., Dal Maso, M., Makela, J. M., Kulmala, M., and O'Dowd, C. D.: Gas-aerosol relationships of $H_2SO_4$, MSA, and OH: Observations in the coastal marine boundary layer at Mace Head, Ireland, J. Geophys. Res.-Atmos., 107(D19), 8100, doi:10.1029/2000JD000229, 2002.

Berresheim, H., Plass-Dulmer, C., Elste, T., Mihalopoulos, N., and Rohrer, F.: OH in the coastal boundary layer of Crete during MINOS: Measurements and relationship with ozone photolysis, Atmos. Chem. Phys., 3, 639–649, 2003.

Bloss, W. J., Evans, M. J., Lee, J. D., Sommariva, R., Heard, D. E., and Pilling, M. J.: The oxidative capacity of the troposphere: Coupling of field measurements of OH and a global chemistry transport model, Faraday Discuss., 130, 425–436, 2005b.

Bloss, W. J., Gravestock, T. J., Heard, D. E., Ingham, T., Johnson, G. P., and Lee, J. D.: Application of a compact all solid-state laser system to the in situ detection of atmospheric OH, $HO_2$, NO and IO by laser-induced fluorescence, J. Environ. Monitoring, 5, 21–28, 2003.

Bloss, W. J., Lee, J. D., Johnson, G. P., Sommariva, R., Heard, D. E., Saiz-Lopez, A., Plane, J. M. C., McFiggans, G., Coe, H., Flynn, M., Williams, P., Rickard, A. R., and Fleming, Z. L.: Impact of halogen monoxide chemistry upon boundary layer OH and $HO_2$ concentrations at a coastal site, Geophys. Res. Lett., 32, L06814, doi:10.1029/2004GL022084, 2005a.

Bloss, W. J., Rowley, D. M., Cox, R. A., and Jones, R. L.: Rate coefficient for the BrO+$HO_2$ reaction at 298 K, Phys. Chem. Chem. Phys., 4 (15), 3639–3647, 2002.

Brauers, T., Hausmann, M., Bister, A., Kraus, A., and Dorn, H. P.: OH radicals in the boundary layer of the Atlantic Ocean 1. Measurements by long-path laser absorption spectroscopy, J. Geophys. Res.-Atmos., 106(D7), 7399–7414, 2001.

Cantrell, C. A., Tyndall, G., and Zimmer, A.: Absorption cross sections for water vapour from 183 to 193 nm, Geophys. Res. Lett., 24, 2195–2198, 1997.

Cape, J. N., Methven, J., and Hudson, L. E.: The use of trajectory cluster analysis to interpret trace gas measurements at Mace Head, Ireland, Atmos. Environ., 34, 3651–3663, 2000.

Carslaw, N., Creasey, D. J., Heard, D. E., Jacobs, P. J., Lee, J. D., Lewis, A. C., McQuaid, J. B., Pilling, M. J., Bauguitte, S., Penkett, S. A., Monks, P. S., and Salisbury, G.: Eastern Atlantic Spring Experiment 1997 (EASE97) – 2. Comparisons of model concentrations of OH, $HO_2$, and $RO_2$ with measurements, J. Geophys. Res.-Atmos., 107(D14), 4190, doi:10.1029/2001JD001568, 2002.

Carslaw, N., Creasey, D. J., Heard, D. E., Lewis, A. C., McQuaid, J. B., Pilling, M. J., Monks, P. S., Bandy, B. J., and Penkett, S. A.: Modelling OH, $HO_2$, and $RO_2$ radicals in the marine boundary layer – 1. Model construction and comparison with field measurements, J. Geophys. Res.-Atmos., 104(D23), 30 241–30 255, 1999a.

Carslaw, N., Jacobs, P. J., and Pilling, M. J.: Modelling OH, $HO_2$, and $RO_2$ radicals in the marine boundary layer – 2. Mechanism reduction and uncertainty analysis, J. Geophys. Res.-Atmos., 104(D23), 30 257–30 273, 1999b.

Chen, G., Davis, D., Crawford, J., Heikes, B., O'Sullivan, D., Lee, M., Eisele, F., Mauldin, L., Tanner, D., Collins, J., Barrick, J., Anderson, B., Blake, D., Bradshaw, J., Sandholm, S., Carroll, M., Albercook, G., and Clarke, A.: An assessment of $HO_x$ chemistry in the tropical Pacific boundary layer: Comparison of model simulations with observations recorded during PEM tropics A, J. Atmos. Chem., 38(3), 317–344, 2001.

Coe, H., Allan, J., Alfarra, M., Bower, K., Flynn, M., McFiggans, G., Topping, D., Williams, P., Dall'Osto, M., Beddows, D., and Harrison, R.: Chemical and physical characteristics of aerosol particles at a remote coastal location, Mace Head, Ireland, during NAMBLEX, Atmos. Chem. Phys. Discuss., 5, 11 643–11 678, 2005.

Creasey, D. J., Evans, G. E., Heard, D. E., and Lee, J. D.: Measurements of OH and $HO_2$ concentrations in the Southern Ocean marine boundary layer, J. Geophys. Res.-Atmos., 108(D15), 4475, doi:10.1029/2002JD003206, 2003.

Creasey, D. J., HalfordMaw, P. A., Heard, D. E., Pilling, M. J., and Whitaker, B. J.: Implementation and initial deployment of a field instrument for measurement of OH and $HO_2$ in the troposphere by laser-induced fluorescence, J. Chem. Soc.-Faraday Trans., 93(16), 2907–2913, 1997.

Creasey, D. J., Halford-Maw, P. A., Heard, D. E., Spence, J. E., and Whitaker, B. J.: Fast photomultiplier tube gating system for photon counting applications, Rev. Sci. Instr., 69(12), 4068–4073, 1998.

Creasey, D. J., Heard, D. E., and Lee, J. D.: Absorption cross-section measurements of water vapour and oxygen at 185 nm. Implications for the calibration of field instruments to measure

OH, $HO_2$ and $RO_2$ radicals, Geophys. Res. Lett., 27(11), 1651–1654, 2000.

Creasey, D. J., Heard, D. E., and Lee, J. D.: Eastern Atlantic Spring Experiment 1997 (EASE97) 1. Measurements of OH and $HO_2$ concentrations at Mace Head, Ireland, J. Geophys. Res.-Atmos., 107(D10), 4091, doi:10.1029/2001JD000892, 2002.

Ehhalt, D. H. and Rohrer, F.: Dependence of the OH concentration on solar UV, J. Geophys. Res.-Atmos., 105, 3565–3571, 2000.

Fleming, Z., Monks, P. S., Rickard, A. R., Heard, D. E., Still, T. J., Sommariva, R., Pilling, M. J., Green, T., Brough, N., Penkett, S. A., Lewis, A. C., Lee, J. D., Saiz-Lopez, A., and Plane, J. M. C.: Peroxy radical chemistry and the control of ozone photochemistry at Mace Head, Ireland during the summer of 2002, Atmos. Chem. Phys. Discuss., 5, 12 313–12 371, 2005.

Haggerstone, A. L., Carpenter, L. J., Carslaw, N., and McFiggans, G.: Improved model predictions of $HO_2$ with gas to partical mass transfer rates calculated using aerosol number size distibutions, J. Geophys. Res.-Atmos., 110, doi:10.1029/2004JD005282, 2005.

Hard, T. M., O'Brien, R. J., Chan, C. Y., and Mehrabzadeh, A. A.: Tropospheric Free-Radical Determination by FAGE, Environ. Sci. Technol., 18(10), 768–777, 1984.

Heard, D. E. and Pilling, M. J.: Measurement of OH and $HO_2$ in the troposphere, Chem. Rev., 103, 5163–5198, 2003.

Heard, D. E., Read, K. A., Methven, J., et al.: The North Atlantic Marine Boundary Layer Experiment (NAMBLEX). Overview of the campaign held at Mace Heard, Ireland, in summer 2002, Atmos. Chem. Phys. Discuss., 5, 12 177–12 254, 2005.

Hofzumahaus, A., Brauers, T., Aschmutat, U., Brandenburger, U., Dorn, H. P., Hausmann, M., Hessling, M., Holland, F., Plass-Dulmer, C., Sedlacek, M., Weber, M., and Ehhalt, D. H.: The measurement of tropospheric OH radicals by laser-induced fluorescence spectroscopy during the POPCORN field campaign and intercomparison of tropospheric OH radical measurements by multiple folded long-path laser absorption and laser induced fluorescence – Reply, Geophys. Res. Lett., 24(23), 3039–3040, 1997.

Holland, F., Hessling, M., and Hofzumahaus, A.: In-Situ Measurement of Tropospheric OH Radicals by Laser-Induced Fluorescence – A Description of the KFA Instrument, J. Atmos. Sci., 52(19), 3393–3401, 1995.

Jenkin, M. E., Saunders, S. M., and Pilling, M. J.: The tropospheric degradation of volatile organic compounds: A protocol for mechanism development, Atmos. Environ., 31, 81–104, 1997.

Kanaya, Y., Matsumoto, J., Kato, S., and Akimoto, H.: Behavior of OH and $HO_2$ radicals during the Observations at a Remote Island of Okinawa (ORION99) field campaign 2. Comparison between observations and calculations, J. Geophys. Res.-Atmos., 106(D20), 24 209–24 223, 2001a.

Kanaya, Y., Sadanaga, Y., Hirokawa, J., Kajii, Y., and Akimoto, H.: Development of a ground-based LIF instrument for measuring $HO_x$ radicals: Instrumentation and calibrations, J. Atmos. Chem., 38(1), 73–110, 2001b.

Kanaya, Y., Yokouchi, Y., Matsumoto, J., Nakamura, K., Kato, S., Tanimoto, H., Furutani, H., Toyota, K., and Akimoto, H.: Implications of iodine chemistry for daytime $HO_2$ levels at Rishiri Island, Geophys. Res. Lett., 29(8), 1212, doi:10.1029/2001GL014061, 2002.

Knight, G. P. and Crowley, J. N.: The reactions of IO with $HO_2$ NO and $CH_3SCH_3$: Flow tube studies of kinetics and product formation, Phys. Chem. Chem. Phys., 3, 393–401, 2001.

Levy, H.: Normal atmosphere: large radical and formaldehyde concentrations predicted, Science, 173, 141–143, 1971.

Lewis, A. C., Hopkins, J. R., Carpenter, L.J., Stanton, J., Read, K. A., and Pilling, M. J.: Sources and sinks of acetone, methanol, and acetaldehyde in North Atlantic marine air, Atmos. Chem. Phys., 5, 1963–1974, 2005.

Logan, J. A., Prather, M. J., Wofsy, S. C., and McElroy, M. B.: Tropospheric chemistry: A global perspective, J. Geophys. Res., 86, 7210–7254, 1981.

Norton, E. G., Vaughan, G., Methven, J., Coe, H., Brooks, B., Gallagher, M., and Longley, I.: Boundary layer structure and decoupling from synoptic scale flow during NAMBLEX, Atmos. Chem. Phys., 6, 433–445, 2006.

Penkett, S. A., Monks, P. S., Carpenter, L. J., Clemitshaw, K. C., Ayers, G. P., Gillett, R. W., Galbally, I. E., and Meyer, C. P.: Relationships between ozone photolysis rates and peroxy radical concentrations in clean marine air over the Southern Ocean, J. Geophys. Res.-Atmos., 102(11D), 12 805–12 817, 1997.

Prinn, R. G., Huang, J., and Weiss, R. F.: Evidence for substantial variations of atmospheric hydroxyl radicals in the past two decades, Science, 292, 1882–1888, 2001.

Read, K. A., Hopkins, J. R., and Lewis, A. C.: Low molecular weight organic compounds in maritime air: Recent results from the NAMBLEX experiment, EGS-AGU-EGU General Assembly, Nice, 2003.

Saiz-Lopez, A. and Plane, J. M. C.: Novel iodine chemistry in the marine boundary layer, Geophys. Res. Lett., 31, L04112, doi:10.1029/2003GL019215, 2004a.

Saiz-Lopez, A., Plane, J. M. C., and Shillito, J. A.: Bromine oxide in the mid-latitude marine boundary layer, Geophys. Res. Lett., 31(3), L03111, doi:10.1029/2003GL018956, 2004b.

Saiz-Lopez, A., Shillito, J. A., Coe, H., and Plane, J. M. C.: Measurements and modelling of $I_2$, IO, OIO, BrO and $NO_3$ in the mid-latitude marine boundary layer, Atmos. Chem. Phys. Discuss., 5, 9731–9767, 2005.

Saiz-Lopez, A., Plane, J. M. C., McFiggans, G., Ball, S. M., Bitter, M., Jones, R. L., Hongwei, C., and Hoffmann, T.: Modelling molecular iodine emissions in a coastal marine environment: the link to particle formation, Atmos. Chem. Phys., 6, 883–895, 2006.

Salisbury, G., Rickard, A. R., Monks, P. S., Allan, B. J., Bauguitte, S., Penkett, S. A., Carslaw, N., Lewis, A. C., Creasey, D. J., Heard, D. E., Jacobs, P. J., and Lee, J. D.: Production of peroxy radicals at night via reactions of ozone and the nitrate radical in the marine boundary layer, J. Geophys. Res.-Atmos., 106(D12), 12 669–12 687, 2001.

Sander, R.: Modelling atmospheric chemistry: Interactions between gas-phase species and the liquid cloud/aerosol particles, Surveys in Geophysics, 20(1), 1–31, 1999.

Sander, S. P., Friedl, R. R., Golden, D. M., Kurylo, M. J., Huie, R. E., Orkin, V. L., Moorgat, G. K., Ravishankara, A. R., Kolb, C. E., Molina, L. T., and Finlayson-Pitts, B. J.: Chemical kinetics and photochemical data for use in atmospheric studies: Evaluation number 14, JPL publication 02–25, 2003.

Schultz, M., Heitlinger, M., Mihelcic, D., and Volzthomas, A.: Calibration source for peroxy-radicals with built-in actinometry using $H_2O$ and $O_2$ photolysis at 185 nm, J. Geophys. Res.-Atmos., 100(D9), 18 811–18 816, 1995.

Simmonds, P. G., Derwent, R. G., McCulloch, A., Odoherty, S., and Gaudry, A.: Long-term trends in concentrations of halocarbons and radiatively active trace gases in Atlantic and European air masses monitored at Mace Head, Ireland from 1987–1994, Atmos. Environ., 30(23), 4041–4063, 1996.

Sommariva, R., Bloss, W. J., Brough, N., Carslaw, N., Flynn, M., Haggerstone, A. L., Heard, D. E., Hopkins, J. R., Lee, J. D., Lewis, A. C., McFiggans, G., Monks, P. S., Penkett, S. A., Pilling, M. J., Plane, J. M. C., Read, K. A., Saiz-Lopez, A., Rickard, A. R., and Williams, P. I.: OH and $HO_2$ chemistry during NAMBLEX: Roles of oxygenates, halogen oxides and heterogeneous uptake, Atmos. Chem. Phys. Discuss., 5, 10 947–10 996, 2005.

Sommariva, R., Haggerstone, A. L., Carpenter, L. J., Creasey, D. J., Carslaw, N., Heard, D. E., Lee, J. D., Lewis, A. C., Pilling, M. J., and Zador, J.: OH and $HO_2$ chemistry in clean marine air during SOAPEX-2, Atmos. Chem. Phys., 4, 839–856, 2004.

Stevens, P. S., Mather, J. H., and Brune, W. H.: Measurement of tropospheric OH and $HO_2$ by laser-induced fluorescence at low-pressure, J. Geophys. Res.-Atmos., 99(D2), 3543–3557, 1994.

Thornton, J. and Abbatt P. D.: Measurements of $HO_2$ uptake to aqueous aerosol: Mass accommodation coefficients and net reactive loss, J. Geophys. Res.-Atmos., 110(D5), doi:10.1029/2004JD005402, 2005.